Nanoscale

PAPER

View Article Online
View Journal | View Issue

Cite this: *Nanoscale*, 2023, **15**, 15008

The cyto-linker and scaffolding protein "plectin" mis-localization leads to softening of cancer cells†

Anahid Amiri, *[a] Christian Dietz, [a] Alexander Rapp, [b] M. Cristina Cardoso[b] and Robert W. Stark[a]

Received 13th May 2023,
Accepted 17th August 2023

DOI: 10.1039/d3nr02226a

rsc.li/nanoscale

Discovering tools to prevent cancer progression requires understanding the fundamental differences between normal and cancer cells. More than a decade ago, atomic force microscopy (AFM) revealed cancer cells' softer body compared to their healthy counterparts. Here, we investigated the mechanism underlying the softening of cancerous cells in comparison with their healthy counterparts based on AFM high resolution stiffness tomography and 3D confocal microscopy. We showed microtubules (MTs) network in invasive ductal carcinoma cell cytoskeleton is basally located and segmented for around 400 nm from the cell periphery. Additionally, the cytoskeleton scaffolding protein plectin exhibits a mis-localization from the cytoplasm to the surface of cells in the carcinoma which justifies the dissociation of the MT network from the cell's cortex. Furthermore, the assessment of MTs' persistence length using a worm-like-chain (WLC) model in high resolution AFM images showed lower persistence length of the single MTs in ductal carcinoma compared to that in the normal state. Overall, these tuned mechanics support the invasive cells to ascertain more flexibility under compressive forces in small deformations. These data provide new insights into the structural origins of cancer aids in progression.

1. Introduction

Cancer begins from oncogene expression[1] and progresses through epigenetic modifications leading to uncontrolled proliferation.[2] The tumor volume expansion is accompanied by angiogenesis/lymph-angiogenesis,[3,4] remodeling of the tumor stroma,[5] and inflammatory-like response of the immune system[6] which collectively impose compressive forces on cancer cells in neoplastic lesions. Cancer cells survive this rigid matrix until the aforementioned mechanical stresses drive cancer invasion actively[7] or by interstitial fluid pressure.[8] Yet, these cells must be resilient enough to extend across the micropores of the tumor foundation which are in the range of 0.1 to 30 μm.[9] In addition, in case we assume that a part of the cancer cells hold static fine-tuned mechanical properties for entering the circulatory system to ascertain a successful metastatic cascade, this would be facilitated if the cell shows easier deformation and is less viscous. It has been more than a decade that studies on cancer cells have resolved these cells' softer bodies compared to those of their healthy counterparts.[10–19] Focus on physical and mechanical dissimilarities between cancerous and healthy single cells unraveled various rheological alterations thereof. These variations involve higher cell motility, lower formation of cell–cell junctions, higher contractile and traction forces, and changes in the cytoskeletal organization of cancerous cells compared to those of their non-transformed counterparts.[20,21]

It is well established that the relative amount of filamentous actin is relevant to the progression of cancer.[20,22] In breast cancer cells the actin network was shown to be less dense and implied fewer stress fibers in the apical perinuclear region and more fibers formed in the basal regions.[20,23] The softening of malignant cells is believed to be linked to changes in cortical actin.[10,24,25] Furthermore, changes in the microtubule network have been monitored in a vast variety of cancers, such as alterations in the expression of tubulin isotypes *e.g.* overexpression of βIII-tubulin which is associated with resistance to chemotherapeutic drugs,[26–34] tubulin post-translational modifications,[35–38] and the expression of microtubule-associated proteins (MAPs).[39–41] Yet, a thorough search of the literature yielded only limited studies focusing on MTs' role in cell rigidity and the results are controversial. While some studies show a minor effect on the cell rigidity when microtubules were disrupted using cytoskeletal drugs,[13,42] others show that microtubule stabilization induced by paclitaxel results in a considerable increase in the overall stiffness[25]

[a]*Physics of Surfaces, Institute of Materials Science, Technical University of Darmstadt, Alarich-Weiss-Str. 2, 64287 Darmstadt, Germany. E-mail: amiri@pos.tu-darmstadt.de*
[b]*Cell Biology and Epigenetics, Department of Biology, Technical University of Darmstadt, 64287 Darmstadt, Germany*

† Electronic supplementary information (ESI) available. See DOI: https://doi.org/10.1039/d3nr02226a

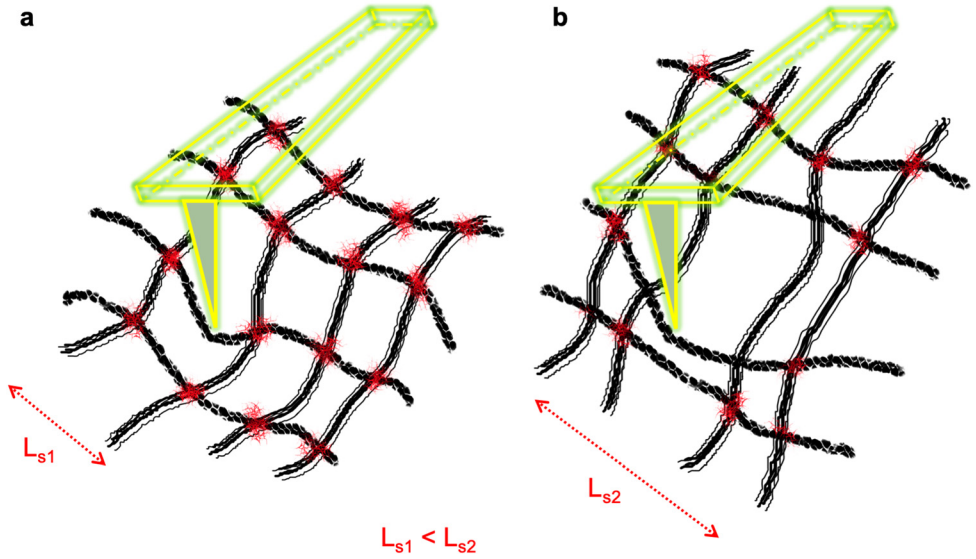

Fig. 1 Schematic diagram of a crisscross network of polymeric meshes. (a) All intersects are joined leading to a confined polymer section (L_{s1}). (b) The mesh is compromised, lacking joints at some intersects leading to a low spatial hindrance for polymer rods with large sections (L_{s2}).

and for suspension cells, at large strains, a significant contribution from the microtubules to cell elasticity was reported.[43–45]

We previously investigated the reason underlying the softening of cancerous cells in comparison with their healthy counterparts based on atomic force microscopy (AFM) with high lateral and spatial precision and fluorescence microscopy (FM). We have shown several epithelial cancer cell lines (invasive ductal carcinoma BT20 cell line, amelanotic melanoma HS695T cell line, liver hepatoma PLC/PRF/5 cell line, and human lung cancer Calu_1 cell line) presenting cytoskeletal distortion while indicating lower stiffness compared to their healthy counterparts[46] or well-differentiated cancer cells.[47,48] In these studies, based on the quantitative nano-mechanical characterization in PeakForce-tapping (PFT-QNM) AFM mode, images of cancerous cells showed scarce cytoskeletal filaments on the cells in direct comparison with the healthy cells. According to the conformational indications, we attributed the lower bending rigidity of cancer cells predominantly to lesser microtubule assembly. The conclusion was based on MTs' mechanical characteristics as a tube with the highest bending strength that can yield more contraction and compression forces among the three types of cytoskeletal filaments. Yet, in this conclusion we had not considered the low indentation depth of around 300 nm into the cells which is due to the limit of oscillation amplitude in PFT mode. This fact questioned the reason for not observing the MTs in the limit of 300 nm indentation depth in cancer cells while their normal counterparts exhibiting a good shield of this network in association with the cells' cortex on top of the cells.

To conceptualize the matter, we consider a polymeric mesh wherein the polymer rods are strongly connected at each cross-link in contrast to a loose polymeric mesh whose polymer rods mostly lie on top of each other, free to slide across each other, rather than making a rigid network. The sketch of these two meshed structures is shown in Fig. 1. It reveals that the network of the loosely jointed polymeric rods shows higher flexibility and mobility under compression force as their spatial hindrance is lower compared to that of a well-crosslinked mesh. The loose network resembles the cancer cells' cytoskeleton and is hypothetically a cause of these cells' lower elastic modulus than that of healthy cells under compression force.

In the supportive cytoskeleton of the cells, the plectin protein, from the plakin family of cytoskeletal linkers, is beneficial in maintaining the structural and mechanical integrity of the cells and tissues against external or internal tensions and stresses. These huge proteins (>500 kDa)[49] cross-link intermediate filaments (IFs) to MTs and F-actin and mediate the attachment of IFs to membrane components,[50,51] stabilize MT organization,[52–54] enable attachment of cell–cell and cell–matrix junctional complexes such as hemidesmosomes and desmosomes, and cause focal adhesions.[55–57] Here, we investigated the cells' cytoskeleton and cyto-linker protein plectin to elucidate this protein's pathological manifestation in breast-type ductal carcinomas and explored its potentially critical role in these cells' lower stiffness compared to that of their healthy counterparts.

2. Results and discussion

2.1. Cytoskeletal filament assessment

2.1.1 Analysis and quantification of the cellular cytoskeleton *via* fluorescence microscopy shows MT disorganization in cancer cells. The actin and MT cytoskeleton of normal epithelial mammary cells (MEC-MCF10a) and breast-type invasive ductal carcinomas (IDC-BT20) were evaluated using the fluorescence imaging technique. One set of images is shown in Fig. 2 (a second sample set of the images is provided in ESI Fig. S1†).

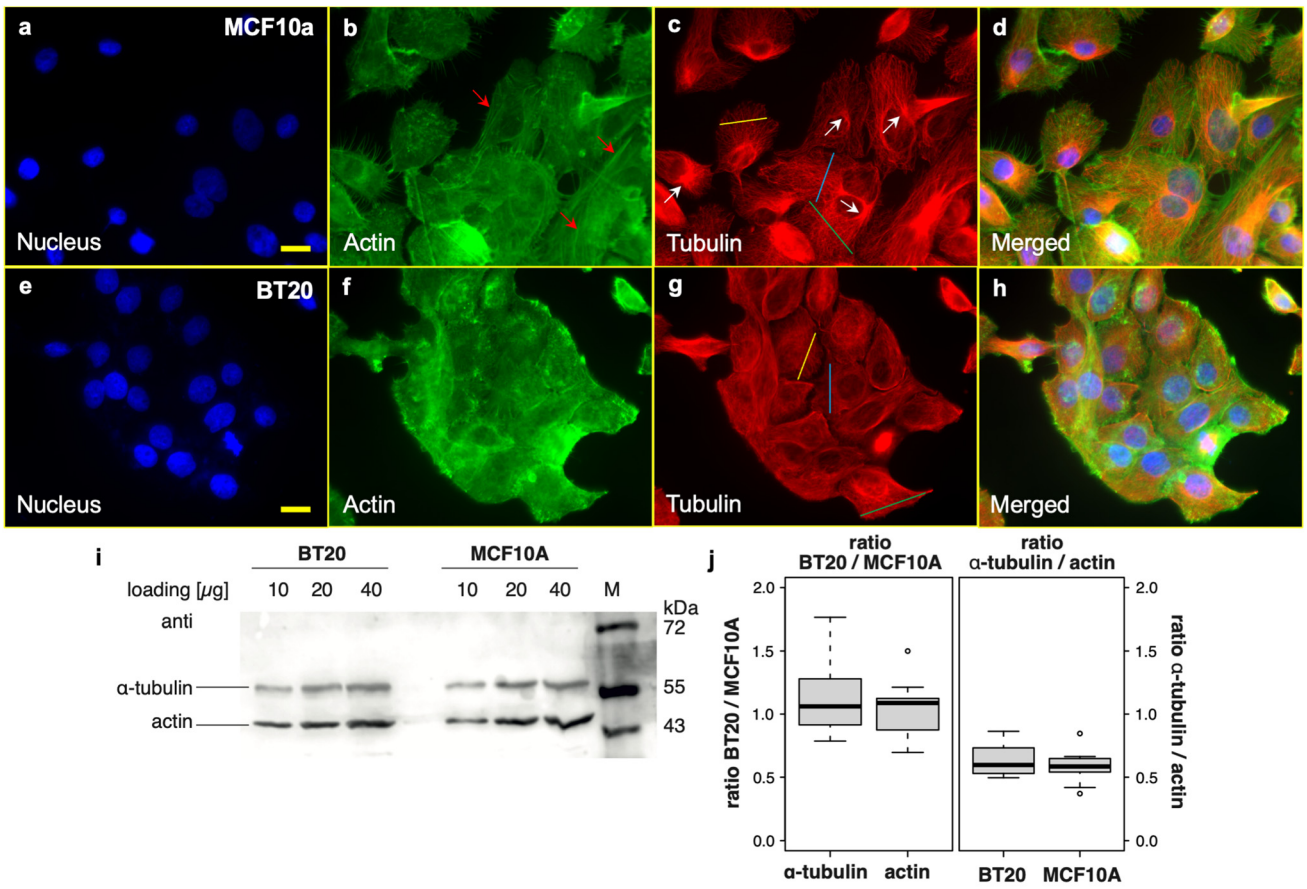

Fig. 2 Fluorescence microscopy images of normal epithelial mammary cells (MCF10a cell line) and ductal carcinomas (BT20 cell line). Cells were stained for filamentous actin (in green) and β-tubulin (in red) and DNA were counterstained with DAPI. (a) Nucleus, (b) F-actin (the red arrows represent the stress fibers formed in the cells), (c) microtubules (the white arrows represent the MTOC location), and (d) merged images of MCF10a cells. (e) Nucleus, (f) F-actin, (g) microtubules, and (h) merged images of BT20 cells. Cross-sections from the MT networks of the two cell lines on (c) and (g) are provided in ESI Fig. S2.† The scale bar is 20 μm. (i) Quantification of the cellular levels of actin and α-tubulin by western blot. Increasing amounts of total protein extracts (10, 20 and 40 μg per lane) were loaded for both cell lines and probed with both, actin and α-tubulin specific antibodies. The expected size of actin is 42 kDa, while that of α-tubulin is 50 kDa. (j) Quantification of four independent replicates (with 2–3 different concentrations each) shows a similar content of both actin and α-tubulin in both cell lines as well as a similar ratio between actin and tubulin. There are no significant differences between the two cell lines (*t*-test).

Upon examining the fluorescence images acquired from BT20 (ductal carcinoma cells) and considering the distinct morphological profiles within this cell population, we observe MTs experiencing bending and tending to form random networks. In contrast, in MCF10a cells, these tubes are oriented radially outward from the microtubule-organizing center (MTOC) (Fig. 2c; the MTOC is marked with white arrows). Furthermore, the MT lattice on BT20 exhibits a fine appearance although densely packed in the cytoplasm, while the well-defined distributed bundles on MCF10a suggest an organized structure of the microtubule network on these cells (representative cross-sections from the MT networks of the two cell lines are provided in ESI Fig. S2†). In addition, the actin stress fibers are absent on BT20 cells (the arrows in Fig. 2b indicate the stress fibers which are formed on MCF10a cells). Yet, all differences considered, the cytoskeleton network is formed on the cancerous cells, potentially serving as an effective shield against external stress. In addition, when quantifying cellular levels of actin and α-tubulin through western blot analysis, both cell lines exhibit a comparable content of both proteins and a similar ratio between actin and tubulin (Fig. 2j). In contrast, our previous AFM-based study demonstrated that the network shield in cancer cells was considerably weaker compared to its healthy counterparts against the applied force (150 pN setpoint force), at which the probe could easily scan the cell nuclei full domain and sense their sub-organelles.[46] Hence, the results from the two imaging techniques indicate a deeper alteration in a cancer cell's cytoskeleton requiring further investigation.

2.1.2 Assessment of the cytoskeletal support along the indentation depth using force–volume mapping characterization mode reveals the cancer specific basal localization of microtubules. To test the cytoskeleton support against force along the indentation depth, we performed experiments on single living cells comparing both normal and cancer cell lines. The force–volume maps were obtained from both cell

lines at the maximum applied force of F = 1 nN which were in accordance with fluorescence microscopy results. The MCF10a cell was stained against F-actin (Fig. 3a) and MTs (Fig. 3b) and measured in the living state in CO_2-independent medium. Fig. 3e and f show cross-sectional profiles (x–z direction) of the local elastic modulus as a function of the z-position at the locations indicated by the cyan lines 1 and 2 in the corresponding F-actin and MT images. The fluorescence image of actin filaments (Fig. 3a) reveals a uniform distribution of this protein mesh covering the cell body. Moreover, the fluorescence image of tubulin filaments (Fig. 3b) depicts a good support of this network all over the cell's body, indicating its protective role in safeguarding the nucleus as well. The cell's MOTC is located at the nucleus where microtubules exhibit a multi-branched network (marked with a red arrow in Fig. 3b). Local elasticity maps (x–z direction) (Fig. 3e derived from line 1, and 3f derived from line 2) show a range from approximately 100 nm to 150 nm of a very stiff part (~10 kPa – yellow portion) at the beginning of indentation to the cell that represents the cell's membrane and cortex with stretched width.

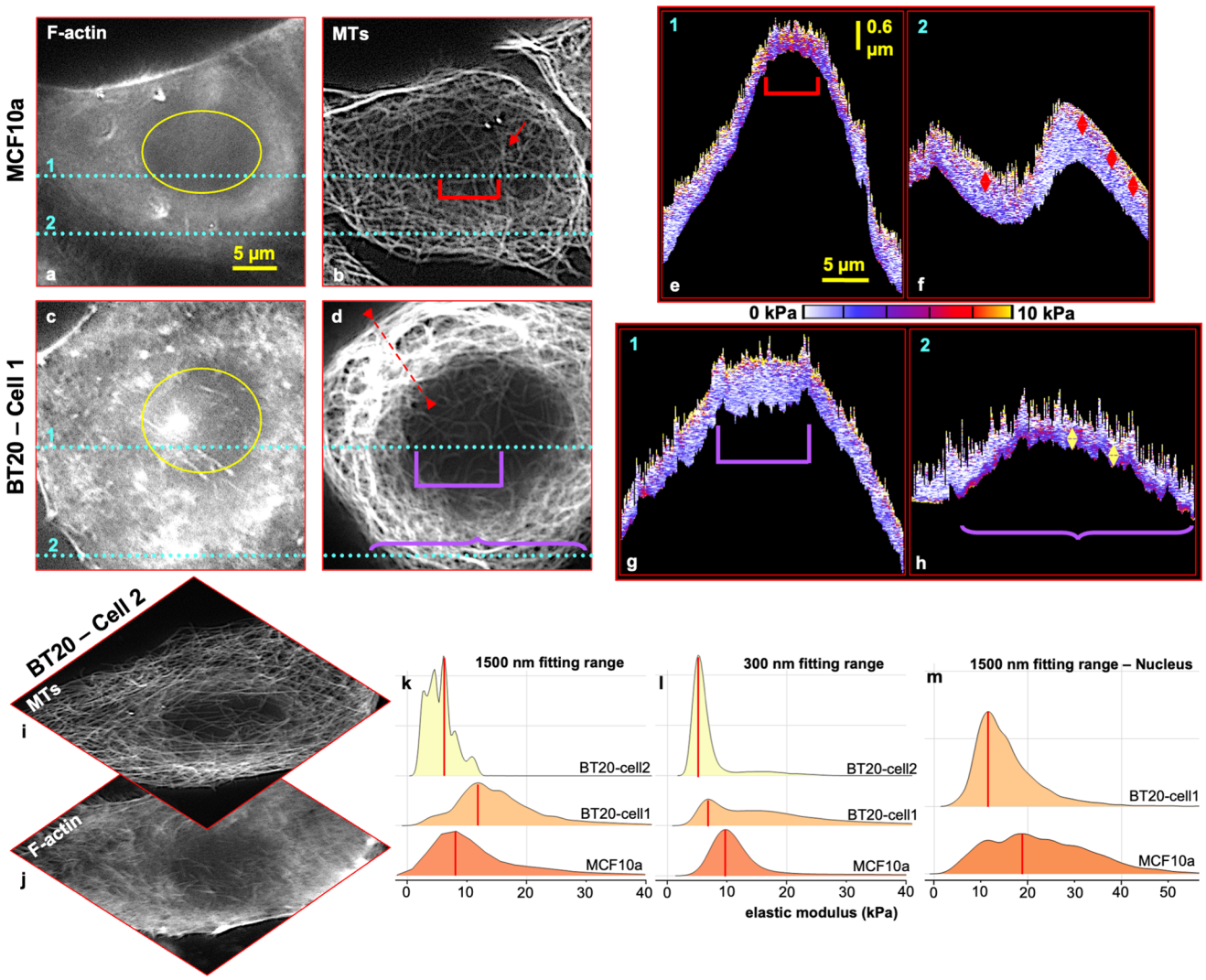

Fig. 3 Live cell force–volume mapping with the trigger point (F = 1 nN) combined with fluorescence imaging. The MCF10a cell was labelled for (a) F-actin and (b) MTs (red arrow shows the MTOC location). Cross-sectional profiles (x–z) of the local elastic modulus as a function of the z-position at the location indicated by the cyan lines 1 and 2 in the F-actin, and MT images are shown in (e) and (f), respectively. The red arrow bars in (f) are 470 nm. The BT20 cell was labelled for (c) F-actin and (d) MTs. Cross-sectional profiles (x–z) of the local elastic modulus as a function of the z-position at the location indicated by the cyan lines 1 and 2 in F-actin, and MT images are shown in (g), and (h), respectively. The yellow arrow bars in (h) are 480 nm. Images (a)–(d) have the same scale bar of 5 µm in the x-plane. Images (e)–(h) have the same scale bar of 5 µm in the x-plane and 0.6 µm in the z-plane. The scale color is segmented for every 2 kPa elevation. A second set of measurements is provided in ESI Fig. S3.† (i) MT and (j) F-actin images of BT20-cell2 which was measured using F–V mapping. BT20-cell2 does not show overrepresentation of the MT network in comparison with BT20-cell1. (k)–(m) Ridgeline plots of kernel smoothed density estimates of the stiffness of MCF10a and BT20 cells acquired from force–volume maps, with (k) a fitting range of 1500 nm (full indentation range) for the full cell body, and (l) a fitting range of 300 nm indentation into the cells for the full cell body, (m) a fitting range of 1500 nm for the nucleus domains marked in (a), for MCF10a cells and (c) for BT20-cell1.

The maximum penetration range of the probe into the cell in the nucleus area was approximately 600 nm (Fig. 3e, red bracket). The cell shows high elasticity along with the full indentation depth in the nuclear region highlighting the significant protection provided by the MT network against the applied force (Fig. 3b and e, areas marked with the red bracket). In the local elastic modulus map (x–z direction) derived from line 2 (Fig. 3f), directly underneath the cortex section (Fig. 3f, top yellow portion), a leveled stiff belt (average stiffness value of 8 kPa) of about 470 nm width is evident (Fig. 3f, marked with red diamonds). From the combined fluorescence image from the cell's MT network (Fig. 3b), it is found that this stiff belt depicts the MT mesh that yields the applied force in support of the cortex.

The BT20 cell was stained against F-actin (Fig. 3c) and MTs (Fig. 3d) and measured in the living state in CO_2-independent medium. Fig. 3g and h show cross-sectional profiles (x–z) of the local elastic modulus as a function of the z-position at the location indicated by the cyan lines 1 and 2 in the corresponding F-actin and MT images. F-actin is highly concentrated in the borders of the cell and is not uniformly spread on the cell. Besides, MTs are over-represented and coiled in the cytoplasm (the red dashed line in Fig. 3d designates the location of the mentioned MTs). The cell's centrosome could not be located and the supportive network of MTs is nearly missing at the rim and on top of the cell's nucleus. Local elasticity maps (x–z direction) (Fig. 3g and h) show a maximum range of approximately ~100 nm for a very stiff (10 kPa – yellow portion) top portion of the cell that represents the blend of the cell's membrane and cortex range. The cell cortex is not uniform and is slightly thinner than that of the healthy cell (~100–150 nm).

The maximum indentation range in the apical nucleus area is approximately 1.2 μm. Its dimensions are indicated by a violet square bracket in Fig. 3d & g. This large indentation range (~1.2 μm) into the nucleus area, in contrast to the healthy cells (600 nm indentation), indicates that the actin network with (on average) a higher elastic modulus than MTs[11] fails to resist the large strain that the tip imposes on the cell's nucleus area where the support from the MT network is compromised.

The local elastic modulus map (x–z direction) (Fig. 3h) derived from position 2 (indicated by the cyan dashed lines in Fig. 3c and d) shows a low indentation range with a maximum of ~600 nm while revealing a stiff tape with a thickness of 120 nm to 480 nm, at the end of the trace trajectory (Fig. 3h, bottom region of the map marked with a purple curly bracket), which deprived the tip from penetrating further. This stiff tape demonstrates the abnormally coiled MT network present in the cancerous cell's body (Fig. 3d, line 2, curly bracket). Unexpectedly, the presented MTs are dissociated from the cortex and placed far lower (around ~400 nm) relative to the cell's cortex and plasma membrane that suggests their basal positioning. This projects an abnormality in the cancer cell's MT network as in the normal state the tubes extend from the centrosome toward the cell cortex and plasma membrane.[58,59]

The reproduced measurements and cell stiffness tomography are provided in ESI Fig. S3.†

Intra-tumor cell population heterogeneity and their morphological differences have been reported in numerous pathological studies.[60–63] This heterogeneity is revealed in the cancer cell stiffness distribution as well (ESI Fig. S4†). Therefore, in our study, we observed that carcinoma cells do not always show a softer mechanical characteristic compared to their healthy counterparts. This is highly influenced not only by the expression level of the cytoskeleton components in the cells but also by the configuration of their network, particularly the MTs. These tube-like filaments bear the major load of resisting under compressive and coupling tensile forces. Fig. 3k depicts the elastic modulus distribution on a single ductal carcinoma with an abnormally coiled MT network (BT20-cell1, Fig. 3d), a nearly well-differentiated single ductal carcinoma with a normal configuration of MTs (BT20-cell2, Fig. 3i) and a single healthy mammary cell, with a fitting range of 1500 nm (the full indentation range into the cells) using the BEC contact mechanics model (bottom effect correction – 2018).[64] This model extracts the true elastic modulus of the soft matter from the force–distance curves by sorting out the reflection of the stiff substrate underneath from the forces detected on the tip, in consideration of the topography.

The stiffness distribution histogram on carcinoma-cell1 in the full indentation range (1500 nm) has a mode value of 11.50–12.00 kPa (median value of 14.38 kPa), and that of carcinoma-cell2 was 5.50–6.00 kPa (median value of 5.34 kPa). The single healthy mammary cell stiffness histogram showed a mode value of 7.50–8.00 kPa (median value of 9.30 kPa).

For a better understanding of the mechanical property differences among the cancer cells we sorted out noninvasive and invasive ductal carcinomas using a Boyden chamber with an 8 μm diameter size porous membrane. We note that all reported errors from median values in the following data are median absolute deviation (MAD). Cancer cells show overall slightly higher stiffness median values of 15.44 kPa (MAD = 6.18 kPa) and 15.31 kPa (MAD = 6.33 kPa) for 20 invasive and non-invasive ductal carcinoma cells, respectively, compared to 20 normal cells with a median value of 14.23 kPa (MAD = 5.05 kPa), in the large deformation range (1500 nm indentation) (stiffness distributions of measured cells and statistics are given in ESI Fig. S5a†). Cancer cells present overly bent and compact polymerized tubulin in the cytoskeleton of the cells, observed by fluorescence microscopy (Fig. 1 and ESI Fig. S2†), which potentially contributes to these cells' higher elastic modulus compared to the MECs with large deformations.

The stiffness of these cells represents an inverted distribution when the cell cytoplasm stiffness values are excluded from the histograms. The stiffness distribution histogram of the carcinoma nucleus has a mode value of 11.50–12.00 kPa and a median value of 13.85 kPa, while the mode value from the histogram of the healthy mammary cell nucleus was 18.50–19.00 kPa with a median value of 21.60 kPa (Fig. 3m). This agrees with the findings that the cytoskeleton, specifically

the MTs network, does not provide a good shield against an external force on top of the cancer cell's nucleus.[46,47] In addition, cancer cell nuclei isolated from the carcinoma cells show lower elasticity compared to healthy mammary cells, with median values of 21.76 kPa (MAD = 13.25 kPa) and 38.10 kPa (MAD = 27.85 kPa), respectively (20 nuclei were measured from each cell line, and the stiffness distribution and statistics of the measured nuclei are given in ESI Fig. S5c†). Given the information mentioned earlier, it's important to exercise caution regarding the outcomes of AFM-based studies that employ colloidal or sharp probes, at which, a single force-distance (FD) curve is captured by positioning the probe over the cell to compare mechanical properties of cancerous and healthy cells. The results from these AFM experiments are highly influenced by the specific location chosen for performing FD spectroscopy.

In view of the basal positioning of the MT network in cancer cells based on stiffness tomography data, we calculated the elastic modulus values on the cells with a fitting range of 300 nm using the BECC model. The stiffness distribution histogram of a single carcinoma cell2 in the shallow indentation range (300 nm) has a mode value of 5.50–6.00 kPa (median value of 14.98 kPa) while that of a single healthy mammary cell was 9.50–10.00 kPa (median value of 10.82 kPa) (Fig. 3l).

Furthermore, accumulative stiffness values with the fitting range of 300 nm of 20 cells from both cell lines were calculated (ESI Fig S5b†). The data show a lower median stiffness value of 8.30 kPa (MAD = 2.70 kPa) for invasive ductal carcinoma than that of noninvasive cells with a median value of 9.59 kPa (MAD = 3.16 kPa). But both cancer cell categories were softer than normal cells with a median value of 12.04 kPa (MAD = 4.71 kPa) in small deformations. The invasive cells show a significant drop in stiffness (in comparison with the full bulk range – 1500 nm stiffness values) of about 7.14 kPa and a similar drop for noninvasive cells of about 5.72 kPa by limiting the deformation range. In consideration of the median stiffness values for the full body of the cells (nucleus and cytoplasm), these results signify the dependence of the acquired stiffness measures on the indentation range while illustrating that the cancer cells are softer only in small deformations in comparison with the normal cells.

In addition, further study on the cell's cytoskeleton support with small deformations using high-resolution imaging by quantitative nanomechanical characterization mapping in PeakForce tapping mode (PFT QNM) on clusters of cells has been carried out and the results and discussion are provided in the ESI.†

2.1.3 Fluorescence microscopy confirms the cancer specific low localization of microtubules. To visualize the distribution of the actin and tubulin cytoskeleton we performed confocal 3D fluorescence microscopy on cancerous and normal mammary cells. Fig. 4a depicts the 3D confocal image of MCF10a cells. The position where the cross-section was drawn through the *x*–*z* plane (Fig. 4b) is illustrated as a horizontal line in Fig. 4a. We observe on the selected cell #1 the MT mesh on top of the nucleus with even distribution of filaments. The orthogonal view in the *y*–*z* direction (Fig. 4c) at the position of the vertical line in Fig. 4a shows the selected cell #2 in which the MTs are situated along the cell surface at the periphery to mechanically support the shape of the cell (quantitative assessment of the 3D images from the MT network in normal cells is provided in ESI Fig. S9a–g†). Furthermore, the mesh of MTs and F-actin are closely associated with each other in the MECs.

Fig. 4d depicts the 3D confocal image taken from BT20 cells. The horizontal line in Fig. 4d illustrates the position

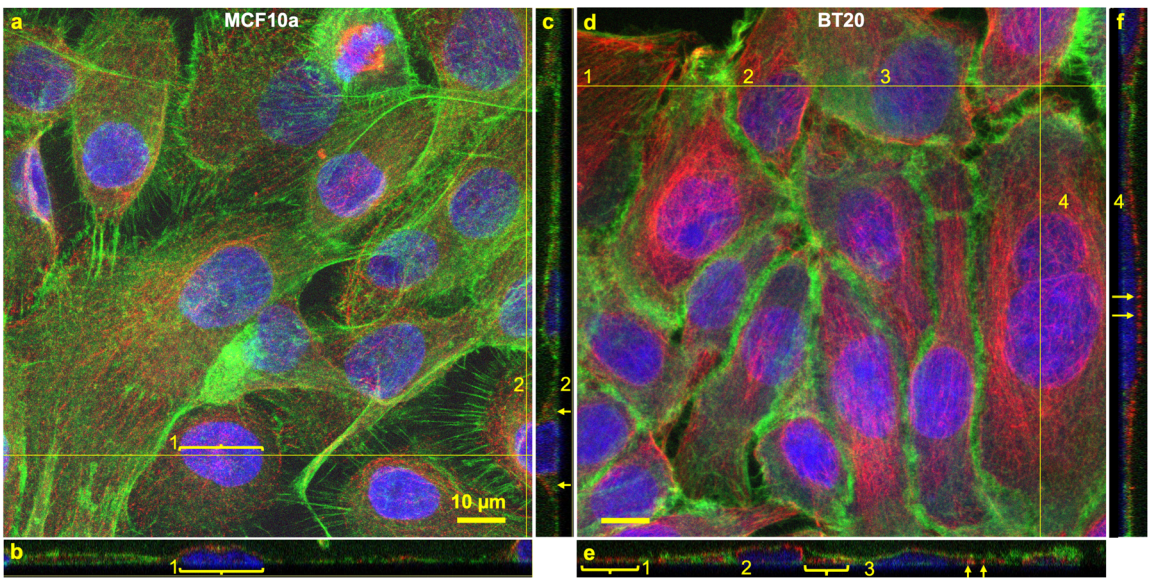

Fig. 4 3D confocal microscopy of MCF10a and BT20 cells. Cells were stained for filamentous actin (in green) and β-tubulin (in red) and DNA was counterstained with DAPI (in blue). MCF10a; (a) *x*–*y* view, (b) *x*–*z* section derived from the position of the horizontal line in (a), and (c) *y*–*z* section derived from the position of the vertical line in (a). BT20; (d) *x*–*y* view, (e) *x*–*z* section derived from the position of the horizontal line in (d), and (f) *y*–*z* section derived from the position of the vertical line in (d).

where the cross-section shown in Fig. 4e (x–z plane) was drawn. All selected cells #1, #2, and #3 show basal location of MTs in the cytoplasm of the cells, and the network is dissociated from the cell's periphery (Fig. 4e, areas marked with arrows and brackets). This supports the prior findings from cancer cells' stiffness tomography (quantitative assessment of the 3D images of the MT network in transformed cells is provided in ESI Fig. S9h–n†). The location where the cross-section through the y–z plane in Fig. 4f was drawn is illustrated by the vertical line in Fig. 4d. The unusually large cell #4 shows over-representation of the MTs on top of the nucleus. Yet the MT skeleton features fully separated individual tubes that may facilitate higher mobility of the mesh under loads. In all cancer cells it is observable that F-actin and MTs are located distant to each other in most parts. This demonstrates the lack of proper crisscross (entanglement) between these cytoskeleton components in the cancer cells.

While the MTs are segmented from the cancer cells' cortex, our data based on the 3D confocal microscopy images (Fig. 4d and ESI Fig. S9h–m, S11, S12†) did not show remodeling of actin filaments or formation of stress fibers in contrast to the results from the study that showed that the MTs were disrupted in the cells using *e.g.*, colchicine.[65] This possibly is due to the fact that the polymer of big size tubulin proteins (50 kDa) is still present in the cancer cells and the cells may respond by reinforcing the cytoskeleton in case the filamentous components are absent.

2.2. Cancer cells' cytoskeletal filament dissociation is a cross-linking failure

In several cancers, plectin mis-localization to the surface of the cell and its dysfunction are reported and claimed to be linked to the cancer cell's invasiveness and metastasis.[66,67] Furthermore, studies show that MTs in P1c-deficient (P1c ($^{-}/^{-}$)) keratinocytes display increased acetylation that leads to changes in cell shape.[53] Furthermore, MTs in plectin gene mutant cells continued to grow and undergo bending at the periphery of the cell.[53,57] Plectin suppression in cells results in a change in centrosomal positioning and its dissociation from the nuclear membrane.[68] The cells' shape abnormality, undirected bending of MTs in their cells' body, and centrosome absence or shifted position are the highlights of the ductal carcinoma cells in our experiments.

Fig. 5 depicts the distribution of the cyto-linker protein, plectin, in ductal carcinoma (BT20) and healthy mammary cells (MCF10a) (second set of epifluorescence microscopy images are provided in ESI Fig. S10†). The expected localization of plectin proteins in normal cells is in the cytoplasm or/and primarily at the periphery of the cells.[66,69,70] Images of MCF10a cell plectin proteins show fulfillment of this expectation and they feature a universal distribution on all the cells. In contrast, BT20 cells show heterogeneity in plectin protein distribution. Some cells show the homogeneous distribution of the protein all over the cells' bodies and nuclei (Fig. 5e, marked with yellow arrows), while in other cells plectins are aggregated on top of the cell's nucleus (Fig. 5e, red arrows). We investigated the positioning of the plectin proteins inside the two cell lines using 3D confocal microscopy with a stack of 30 slices with ~300 nm axial resolution. Fig. 5g–l illustrate maximum intensity projections of image stacks of 6 frames from MCF10a cells. The integrated intensity of plectin in the z-direction of 6 cells (Fig. 5m, derived from the squares marked in Fig. 5g–l) shows uniform distribution of plectin proteins in the cells' cytoplasm with a peak intensity near or at the midpoint of the cells' volume. The 3D confocal microscopy results on BT20 cells are illustrated in Fig. 5n–s, which show maximum intensity projections of the image stacks of 6 frames. The integrated intensity of plectin in the z-direction of 6 cells (Fig. 5t, derived from the squares marked in Fig. 5n–s) shows apical positioning of the plectin proteins in cancer cells.

It is worth noting that the aggregation of proteins provides a comparably stiff response as observed by atomic force spectroscopy. Thus, the centralization of plectin proteins on top of the nucleus domain is observable in the AFM images through a change in elasticity and/or energy loss. The oscillation trajectory in PFT QNM-AFM is sinusoidal causing the peak velocity of the cantilever to be at the middle position of the oscillation. This allows for relatively high-speed imaging while for maintaining the image resolution, the oscillation amplitude of the probe in PFT-QNM mode is limited to max. 300 nm. The small oscillation amplitude eventually limits the maximum indentation of the tip into the samples to be around 300 nm (ESI Fig. S7†).

Considering the shallow indentation limit of the probe into the cell and its capability of recording super high-resolution spectra, it is credible to employ this mode for further study of plectin protein physiological manifestation in the cancer cells. For this aim, we characterized the ductal carcinoma cells in living state for a duration of around an hour using PFT QNM mode and instantly fixed and stained the cells against plectin proteins after the AFM measurements. Fig. 6a and b depict two living round shaped BT20 cells with fairly different heights showing high elasticity in the center of the nucleus domains (Fig. 6c, representative height and elastic modulus cross sections derived from the location in Fig. 6a and b). These two cells exhibit aggregation of plectin proteins on top of the nuclei in fluorescence images (Fig. 6d–f). Considering the low indentation range of about 300 nm into the sample in PFT QNM mode it is valid to conclude that plectin proteins are apically positioned and they also form a firm aggregate on top of the nucleus.

Heterogeneity is a hallmark of cancer and is apparent in plectin protein distribution in these cells as well (Fig. 5, and ESI Fig. S10†). In contrast to the first case, some BT20 cells show an even distribution of plectin proteins on the cell body and nucleus. For monitoring the behavior of the latter cells under force, two morphologically different (polygon shaped) BT20 cells are chosen to be measured in living state (Fig. 6g, and h). The elastic modulus values on the nucleus domains of these cells show an even distribution (Fig. 6i, representative height and elastic modulus cross sections derived from the location in Fig. 6g and h), while the fluorescence images

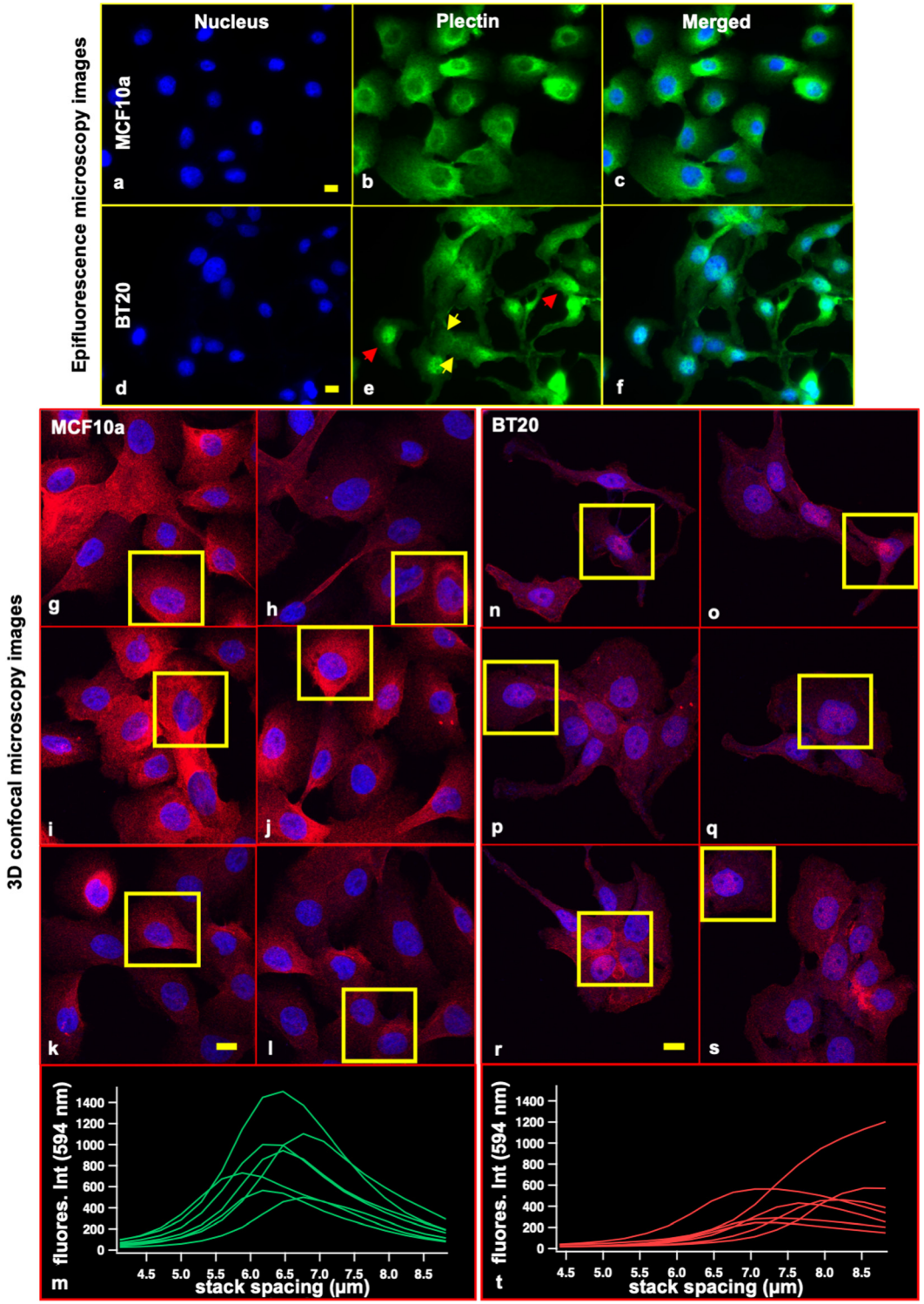

Fig. 5 Fluorescence microscopy images of cyto-linker plectin proteins; epifluorescence microscopy: (a) nucleus, (b) plectin proteins, (c) merged image of normal mammary cells (MCF10a cell line). (d) Nucleus, (e) plectin proteins, and (f) merged image of ductal carcinomas (BT20 cell line). (g)–(l) Maximum intensity projections of 3D confocal microscopy image stacks containing 30 slices each of the plectin proteins in MCF10a cells. Plectin staining is shown in red and nuclear DNA is counterstained with DAPI and shown in blue. The yellow squares illustrate the selected cells for plectin protein assessment in the cells' volume. (m) Integrated intensity of plectin in the *z*-direction. The cells show uniform distribution of plectin proteins in the cell body with a peak intensity near or at the middle of cells' volume. (n)–(s) Maximum intensity projections of 3D confocal microscopy image stacks containing 30 slices each of the plectin proteins in BT20 cells. Plectin staining is shown in red and nuclear DNA is counterstained with DAPI and shown in blue. The yellow squares illustrate the selected cells for plectin protein assessment in the cells' volume. (t) Integrated intensity of plectin in the *z*-direction. The cells show the distribution of plectin proteins near the surface of the cells. This confirms these proteins' apical positioning in cancer cells. The scale bar is 20 μm.

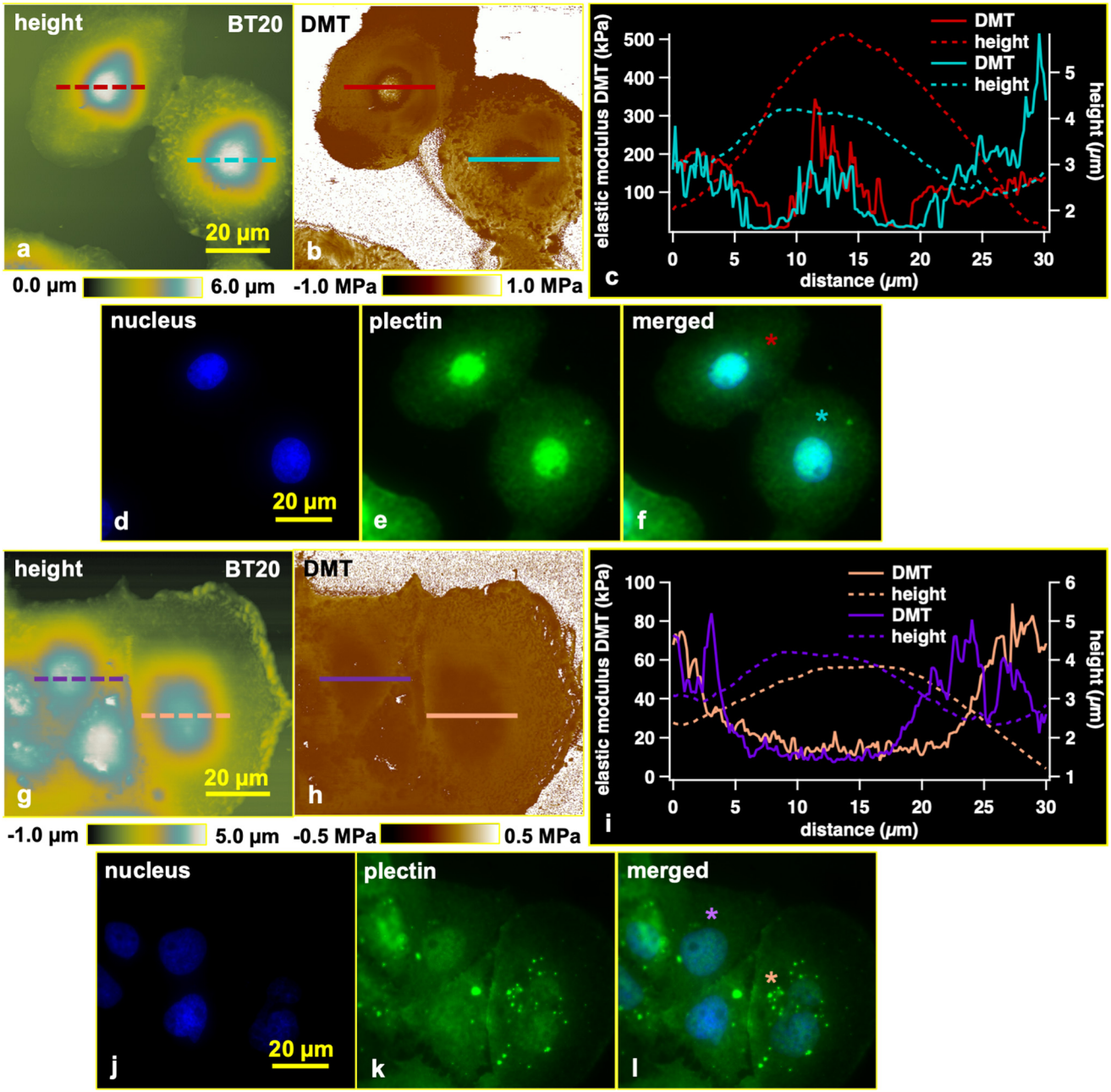

Fig. 6 Living BT20 cell AFM measurements followed by fluorescence microscopy. Cells were stained against plectin proteins (in green) and DNA was counterstained with DAPI (in blue). (a) Height image, (b) DMT image of BT20 cells with a central stiff nucleus domain due to plectin aggregation shown in (c) the height profile and stiffness distribution derived from the locations marked in (a) and (b). Cells were instantly fixed and stained after the AFM measurement; (d) nucleus, (e) plectin protein, and (f) fluorescence merged image. (g) Height image, (h) DMT image of BT20 cells with smooth stiffness distribution on the nucleus domain illustrated in (i) the height profile and stiffness distribution derived from the locations marked in (g) and (h). (j) Nucleus, (k) plectin protein, and (l) fluorescence merged image.

confirm the nearly uniform spread of plectin proteins on the cells' body and nucleus (Fig. 6j–l).

In view of the above-mentioned plectin-related disorders and the information provided by our experiments, the mislocalization of plectin proteins and their centralized apical positioning in the carcinomas signify a disruption in these proteins' task fulfillment as the main crosslinker of the cytoskeleton of the cells. This might lead to impaired crosslinking of the cytoskeletal filaments over the cell's body and disengaged MTs (broken IF–MT bridges). We segregated the invasive and noninvasive ductal carcinoma cells using a Boyden chamber with 8 μm membrane pores and performed *z*-stacks using confocal imaging on each cancer cell category stained against F-actin, α-tubulin and plectin proteins (ESI Fig. S11 and S12†). Remarkably, only invasive cells show aggregation of plectin proteins on the nucleus domains and uneven distri-

bution of the plectin proteins in cells' body (ESI Fig. S11d, i and n,† marked with yellow arrows), while noninvasive cell plectin proteins are evenly spread all over the cells' body and nuclei (ESI Fig. S12†). The orthogonal views of invasive cells feature more flattened morphology in comparison with the noninvasive cells (Fig. 7). In the invasive cells (Fig. 7a) MTs (indicated by red) are positioned basally and very poorly covering the nuclei, and plectin proteins (indicated by magenta) are present on top of the nuclei (marked with asterisk in Fig. 7a). In contrast, noninvasive cells show, in some cases, compact MTs in cells' body (marked with asterisks in Fig. 7b) which strongly manifested over the nuclei as well.

We carried out several control force spectroscopy measurements to distinctly examine the pivotal role of each cytoskeleton component in cells' mechanical integrity. In one group of controls normal mammary epithelial cells (MEC-MCF10a) were treated with cytochalasin-D drug for disrupting the actin filaments, in the second group colchicine was added to induce MT disassembly and in the third group MCF10a cells were transfected with siRNA targeting the plectin proteins. The median BECC elastic modulus values for small and large deformations are provided in Table 1. The violin plots of kernel smoothed density estimates of the stiffness can be found in ESI Fig. S13.† For a small deformation range (300 nm) F-actin was disrupted and cyto-linker plectin deficient cells appeared with a drastic decrease in the elastic moduli compared to the intact MECs (7.07 kPa, 7.56 kPa, 12.04, respectively). This shows either F-actin collapse or cyto-linker absence, and the cortex of the cell becomes highly flexible. Also, we observe that in the absence of MT support under the cortex of the cell (colchicine-treated), F-actin roughly fails to keep the cells' cortex mechanical integrity (a decrease from 12.04 kPa to 9.80 kPa). Remarkably, in a large deformation range (1500 nm) the significant role of MTs in supporting the cells' stiffness is evident, as cells show the softest form among all control cases when MTs are disrupted. Here we note that there is a major discrepancy among the biophysics community reports on the MT disruption effect on cell stiffness due to employing conventional contact mechanic models which do not consider the bottom-effect-artifacts (see elastic modulus distributions produced with the DMT model in ESI Fig. S13d†).

While both invasive and noninvasive ductal carcinoma cells show very close stiffness values in full bulk consideration (1500 nm fitting range, 15.44 kPa, and 15.31 kPa, respectively), the lower median stiffness value of the invasive cells (8.30 kPa) in comparison with that of noninvasive ones (9.59 kPa) on a small deformation scale is justified majorly by basal positioning of MTs in invasive cells which was earlier argued.

In the light of the above arguments and the results from the 3D confocal imaging and the control stiffness measurements, we concluded that the plectin mis-localization in invasive cells causes segmentation in cyto-linking which in turn leads to MTs parting from the cell's cortex and basal localization of these tubes in cancer. This tuned mechanics helps the invasive cells in the progression and intravasation of the anatomical spaces.

2.3. Microtubule persistence length assessment

2.3.1 High resolution imaging of the MTs using AFM unravel the lower persistence length of these filaments in the cancer state. Bending persistence length (l_p) is the segment length of a polymer at which the orientation of its bonds persists and below that it can be approximated as a rigid rod. This provides a useful quantitative measure of a polymer's stiffness. In case l_p is smaller than the polymer contour length (L), the polymer is more flexible, if the l_p and L are comparable, the polymer is considered semiflexible, and when the l_p is larger than the L the polymer acts like a rigid rod. We provided a schematic illustration of polymers with various l_p in Materials and methods (4.7.2 Persistence length assessment, Fig. 9a–c).

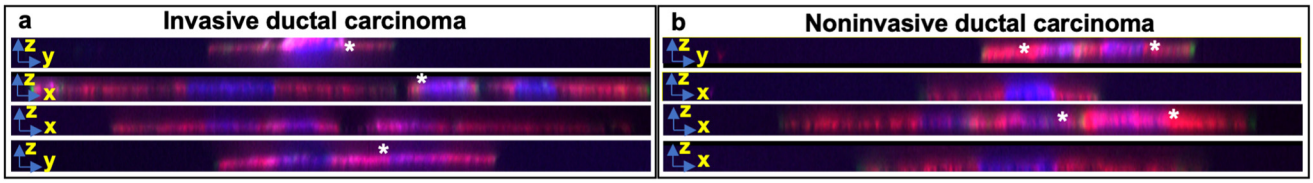

Fig. 7 3D confocal microscopy of ductal carcinoma cells (BT20). (a) Orthogonal views of invasive cells and (b) orthogonal views of noninvasive cells. Cells were stained for filamentous actin (CellMask actin-tracking) (in green), α-tubulin (in red), and plectin proteins (in magenta), and DNA was counterstained with DAPI (in blue). The location at which these views are derived from are marked in ESI Fig. S11 and S12† (merged images).

Table 1 Effect of cytoskeleton components on cell mechanical integrity. Median stiffness values measured based on the BECC model

Deformation range	MEC (MCF10a) (kPa)	Cytochalasin-D treated (kPa)	Colchicine treated (kPa)	Plectin siRNA transfected (kPa)	Invasive ductal carcinoma (BT20) (kPa)	Noninvasive ductal carcinoma (BT20) (kPa)
300 nm	**12.04** (MAD = **4.71**)	**7.07** (MAD = **2.10**)	**9.80** (MAD = **2.35**)	**7.56** (MAD = **2.11**)	**8.30** (MAD = **2.70**)	**9.59** (MAD = **3.16**)
1500 nm	**14.28** (MAD = **5.05**)	**13.39** (MAD = **4.78**)	**12.83** (MAD = **4.01**)	**13.98** (MAD = **6.20**)	**15.44** (MAD = **6.18**)	**15.31** (MAD = **6.33**)

Given that cytoskeletal filaments are thick polymers and are governed by their bending energy, they are considered to be generally semiflexible in normal cells, but by focusing on the MT configuration using fluorescence microscopy (ESI Fig. S14†), it becomes clear that these tubes show emphasized coiled shapes in cancer cells which is against their nature of having a straight lattice in the normal stable state. Previous studies on the dynamics of MTs found curved protofilaments (PFs) at the tip of depolymerizing MTs, therefore portraying the curvature as an indication of instability in MTs and revealing its catastrophe state.[71–73] Other studies found a curved conformation of PFs in both GTP- and hydrolyzed GTP-capped cases.[71,72,74] The curved–straight transition of the PFs is in general the competition of the dimer's bent spring tendency with lateral interaction forces. Nevertheless, cancerous cells' MTs seem to overcome the lateral forces and favor strongly curved configurations that need further investigation. Yet, from the mechanical point of view, these coil shape single tubes suggest MTs with a lower l_p than the contour length which indicates a flexible polymer. We have imaged sections of the cancerous and healthy cells with very high resolution of 2 nm per pixel using nanomechanical characterization mapping to spot the MTs in the cells. The cells' F-actin was disrupted using cytochalasin-D to facilitate easier localization of the MTs in the images and cells were instantly fixed prior to the experiments. The representative images of 5 cell scans from each cell line are illustrated in Fig. 8 (the other 4 scans from each cell line are provided in ESI Fig. S15†). For not mixing the MTs with intermediate filaments we first located the centrosome in each cell line and assessed the configuration of the tubes and bundles (Fig. 8b and e). In normal cells the centrosome was found adjacent to the nucleus (Fig. 8a, box

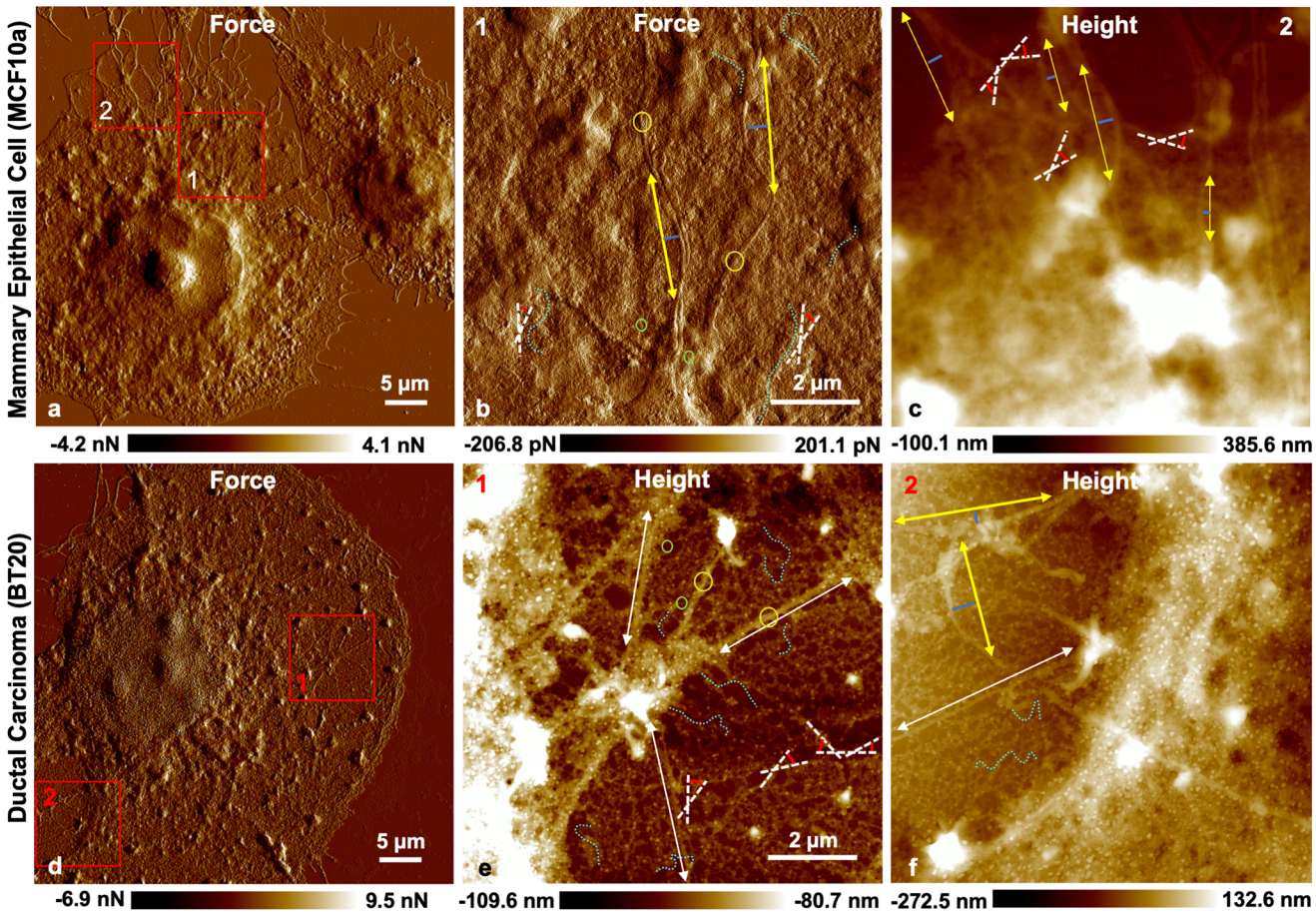

Fig. 8 PFT QNM-AFM. (a) PeakForce error full image of a MCF10a cell with a scan size of 92 × 92 μm^2 and a low resolution of 180 nm per pixel, (b) PeakForce error image of the centrosome, zoomed-in in the area of box 1 in (a) with a scan size of 10 × 10 μm^2 and a high resolution of 2 nm per pixel, (c) height images of MTs in the cytoplasm of the cell, zoomed-in in the area of box 2 in (a) with a scan size of 10 × 10 μm^2 and a high resolution of 2 nm per pixel. (d) PeakForce error full image of a BT20 cell with a scan size of 92 × 92 μm^2 and a low resolution of 180 nm per pixel, (e) height image of the centrosome, zoomed-in in the area of box 1 in (d) with a scan size of 10 × 10 μm^2 and a high resolution of 2 nm per pixel, (f) height images of MTs in the cytoplasm of the cell, zoomed-in in the area of box 2 in (d) with a scan size of 10 × 10 μm^2 and a high resolution of 2 nm per pixel. Cyan dashed curves illustrate the conformation of the tubes in (b) and (e) and the circles represent the location from which the height profile of the tubes is obtained (ESI Fig. S16†). White dashed lines in (b), (c), and (e) are representative of tangent–tangent correlation, and the yellow line with the corresponding blue normal lines in (b), (c), and (f) are representative of the beam deflection model and the white lines in (e) and (f) are representative of straight tube estimate. Images were taken with a setpoint of 10 nN, with an oscillation frequency of 2 kHz and an oscillation amplitude of 100 nm. Scan rate was set to 0.1 Hz.

1) while in cancer cells either it was shifted in position (Fig. 8d, box 1) or absent. The MTs' bundles in both cell lines depict a full-width-at-half-maximum of 100–120 nm and that of the tubes was 25–32 nm (the height profiles are given in ESI Fig. S16;† the circles in Fig. 8b and e are the locations from which the height profiles are derived). In the AFM images the tubes maintain both an average planar/straight conformation and various curved shapes. We note with our common understanding, the term "straight" refers to the length scale over which a polymer does not change direction. The worm-like-chain (WLC) model[75] is the most commonly used continuum description for characterizing nano-mechanics and thermodynamics of biopolymers, in which the l_p of the chains is defined by the characteristic length scale (s) for the exponential decay of the two-point correlation function between unit tangent vectors (t) along the polymer (Fig. 9e). For $L \gg l_p$ the WLC behaves like an ideal chain with discrete N numbers. Therefore, here, we used the freely jointed chain model cosine correlation function for the flexible tubes for measuring the l_p given by:[76–78]

$$\langle \cos(\vartheta(s) - \vartheta(0)) \rangle = e^{-\frac{s}{2l_p}} \quad (1)$$

where $\vartheta(s)$ is the tangent angle at coordinate (s) and $\vartheta(0)$ is the reference tangent angle.

Furthermore, assuming that the WLC is well approximated as an inextensible filament (*e.g.* compliance of the cell is due to filaments bending and sliding over each other and not their extension), we calculated the l_p from the freely jointed beam deflection model (bending mode) by means of the deviation of size δ from a straight line of correlation length ξ (end-to-end approach, sum of all discrete chains, schematic illustration is provided in Fig. 9d) given by:[78,79]

$$\langle \delta^2 \rangle = \frac{\xi^3}{48 l_p} \quad (2)$$

In addition, the straight bundles are estimated by following their contour length. The calculation of 80 segments of MTs (40 tubes, 40 bundles) were carried out from 5 cells out of each cell line (Table 2). The average of the bundles l_p is slightly higher in normal cells than that in cancer cells (6.49×10^{-6} m $\pm$ 1.02×10^{-5} m and 5.99×10^{-6} m $\pm$ 1.23×10^{-5} m, respectively; note that the large standard deviation only emphasizes the large distribution of filament persistence lengths in cells). Yet, the main difference between these two cell line MT lattices manifests in their single tubes. The single MTs in Fig. 8b (depicted by cyan dashed curves) exhibit an open curved conformation in normal cells while the single tubes in Fig. 8e (depicted by cyan dashed curves) feature a compact and coiled conformation in cancer cells. These observations are in good agreement with the prior fluorescence measurements (ESI Fig. S14†). The average value of l_p of single MTs in cancer cells is calculated to be around 360 nm and it is less than that of healthy cells (Table 2, 3.93×10^{-7} m $\pm$ 3.07×10^{-7} m, and 7.51×10^{-7} m $\pm$ 6.47×10^{-7} m, respectively).

MTs are characterized as a very stiff rod with persistence length in the range of 1–8 mm.[80–82] Yet, the shear modulus of the MTs is reported to be largely lower than their elastic modulus[83,84] due to weaker inter-protofilament bonds than protofilament head-to-tail bonds that allow them to slide on one another.[85,86] This implies that the flexural rigidity and in consequence the l_p is contour-length-dependent and studies show that, as a result, MTs have l_p values one to two orders of magnitude shorter on shorter scales than those in earlier reports.[83,87] Our data are in accordance with the latter reports.

We believe that the lower l_p of MTs in cancer cells leads to a more flexible behavior of individual tubes under compressive forces than semiflexible chains present in the normal cell MT lattice. In addition to the basal location of the MTs in cancer cells, the lowered l_p of these cells' tubes can also effectively aid the cancer cells in squeezing through the micropores and facilitate cancer to invade surrounding tissues.

Table 2 Persistence length of MTs and MT bundles, *in situ*

Cell line	ℓ_p (for $L > \ell_p$) (m)	ℓ_p (for $L \leq \ell_p$) (m)	ℓ_p (total) (m)
MCF10a	7.51×10^{-7} $\pm$ 6.47×10^{-7}	6.49×10^{-6} $\pm$ 1.02×10^{-5}	3.81×10^{-6} $\pm$ 7.97×10^{-6}
BT20	3.93×10^{-7} $\pm$ 3.07×10^{-7}	5.99×10^{-6} $\pm$ 1.23×10^{-5}	3.36×10^{-6} $\pm$ 9.33×10^{-6}

3. Conclusions

We investigated the mechanism underlying the softening of cancerous cells in comparison with their healthy counterparts based on AFM high resolution stiffness tomography and 3D confocal microscopy. We studied breast type cancerous and healthy epithelial mammary cells in this work. Our data illustrate an abnormality in the invasive ductal carcinoma MT network. Fluorescence images from the network show overly bent tubes and a compact lattice in the cytoskeleton of the cells while the centrosome is absent or shifted in position. The stiffness tomography, in addition, depicts the basal location of the MT network in the IDC cell cytoskeleton while being segmented for around 400 nm from the cell cortex and plasma membrane. Nevertheless, in normal cells the MT network is situated in the cells' periphery supporting the cells' cortex. These observations are confirmed by means of 3D confocal microscopy from both cell lines in this study.

Cell cytoskeletal filaments are interconnected in the periphery exploiting a cyto-linker protein, so called plectin, to maintain the mechanics of the cells. The peripheral localization of plectin proteins in normal epithelial mammary cells (MCF10a) and their good cytoskeletal filament association observed by 3D confocal microscopy and cell stiffness tomography confirm their mechanical and scaffolding integrity. Yet, the cytoskeleton scaffolding plectin proteins are located apically in the form of aggregates on top of the nucleus in invasive carcinomas. Apical positioning of plectin in these cells indicates a disruption in their scaffolding function in the periphery which causes a failure in maintaining the MTs right beneath the plasma membrane and cell's cortex.

In addition, the single MTs in ductal carcinomas showed lower persistence length in comparison with normal cells' MTs. Overall, the fragmented crosslinking of cytoplasmic filaments and lowered persistence length of the MTs help the invasive cells in becoming more flexible under compressive forces with small deformations and aid them in migrating through tight anatomical spaces more efficiently in the metastasis cascade.

4. Materials and methods

4.1 Cell culture

Ductal carcinoma cells (BT20 cell line) received from CLS Cell Lines Service GmbH (Eppelheim, Germany) and normal mammary epithelial cells (MCF10a cell line; Research Resource Identifiers RRID CVCL_0598) were used in this study. BT20 cells were cultured at first in tissue culture flasks in DMEM/F-12 media (50 : 50 vol : vol) from Thermo Fisher Scientific (Thermo Fisher Scientific, Germany) containing 10% FBS (Merck KgaA, Darmstadt, Germany) and 1% penicillin/streptomycin (Carl Roth GmbH+Co. KG, Karlsruhe Germany) and MCF10a cells were cultured in DMEM/F-12 media (50 : 50 vol : vol) from Thermo Fisher Scientific containing 10% FBS (Merck KgaA, Darmstadt, Germany), 1% penicillin/streptomycin (Carl Roth GmbH+Co. KG, Karlsruhe Germany), 20 ng ml^{-1} EGF (Peprotech, Germany #AF-100-15), 0.5 mg ml^{-1} hydrocortisone (Merck KgaA, Darmstadt, Germany, #H-0888), 100 ng ml^{-1} cholera toxin (Merck KgaA, Darmstadt, Germany, #C-8052), and 10 μg ml^{-1} insulin (Merck KgaA, Darmstadt, Germany, #I9278). We used trypsin/EDTA (Thermo Fisher Scientific, Germany #25300062) to detach the cells, and subsequently centrifuged and seeded them on glass coverslips/slides for the experiments and incubated at 37 °C/5% CO_2.

4.2. Cell staining

4.2.1 Cytoskeleton – fixed cells. Cells were fixed with 3.7% formaldehyde diluted in PBS for 15 min followed by 15 min permeabilization with 0.2% Triton X-100 in PBS at RT. Afterwards, the cells were blocked to avoid non-specific binding by means of 1% bovine serum albumin (BSA) in PBS and incubated for 20 min at RT. Cells were incubated in primary antibody mouse monoclonal anti-β-3 tubulin (#2 28 33) (Thermo Fisher Scientific, Germany) or mouse-anti-α tubulin (Sigma Aldrich Clone DM1A) diluted in blocking solution at a ratio of 1 : 200 at RT for 1 h. The cells were washed 3 times using PBS. Afterwards the cells were incubated for 1 h in the secondary antibody AlexaFluor 594 conjugated goat-anti-mouse (#A32744) (Thermo Fisher Scientific, Germany) which was diluted in blocking solution at a ratio of 1 : 1000. The F-actin network was stained for 15 min using CellMask Actin-Tracking green (#A57249) (Thermo Fisher Scientific, Germany) diluted in blocking solution at a ratio of 1 : 1000 and counterstained with DAPI (Thermo Fisher Scientific, Germany) which was diluted in blocking solution at a ratio of 1 : 1000 at RT.

4.2.2 Cytoskeleton – living cells. Prior to AFM experiments, cells were loaded with CellMask actin-tracking green and tubulin-tracker deep red (Thermo Fisher Scientific, Germany, #A57243 and #T34077, respectively) at a ratio of 1 : 1000 in FluoroBrite DMEM (Thermo Fisher Scientific, Germany, # A1896701) for 40 min in a 37 °C/5% CO_2 incubator and washed with probenecid (77 mg ml^{-1}) containing buffer (1 : 1000) to minimize the efflux of the probe during washing and imaging.

4.2.3 Plectin proteins – fixed cells. Cells were fixed with 3.7% formaldehyde diluted in PBS for 15 min followed by 15 min permeabilization with 0.2% Triton X-100 in PBS at RT. Afterwards, the cells were blocked to avoid non-specific binding by means of 1% bovine serum albumin (BSA) in PBS and incubated for 20 min at RT. The cells were incubated in primary rabbit-anti-plectin antibody (Thermo Fisher Scientific, Germany, #SY29-04), diluted in blocking solution at a ratio of 1 : 200 at RT overnight, and later the samples were washed 3 times using PBS and incubated for 1 h in secondary antibody goat-anti-rabbit Alexa Fluor 488 (Thermo Fisher Scientific, Germany, #A48282) or goat-anti-rabbit Alexa Fluor 647 (Thermo Fisher Scientific, Germany, #A21245) which were diluted in blocking solution at a ratio of 1 : 1000 and counterstained with DAPI (Thermo Fisher Scientific, Germany) at a ratio of 1 : 1000 in blocking solution at RT.

For the second round of experiments (shown in ESI Fig. S13†), cells were fixed at −20 °C in 100% methanol and were incubated in primary rabbit-anti-plectin antibody (Thermo Fisher Scientific, Germany, #SY29-04) as described above. The samples were washed 3 times with PBS and incubated for 1 h in secondary antibody goat anti-rabbit Alexa Fluor 488 (Thermo Fisher Scientific, Germany, #A48282) which was diluted in blocking solution at a ratio of 1 : 1000 without DAPI.

4.3 Control measurements

4.3.1 Colchicine and cytochalasin-D treatment. In actin depolymerization experiments, cells were incubated for 30–40 min with 5 μg ml^{-1} cytochalasin-D (Merck KgaA, Darmstadt, Germany, #C8273) prior to AFM measurements. Cytochalasin-D was kept as a stock solution of 1 mg ml^{-1} in dimethyl sulfoxide (DMSO) at −20 °C. In MT disruption experiments, cells were incubated for 1.5 h with 50 μg ml^{-1} colchicine (Merck KgaA, Darmstadt, Germany, #C9754) prior to AFM measurements. 0.5 g colchicine per 100 ml in sterile distilled water was kept as a stock solution at room temperature in the dark. Before applying the drug to the cells, they were incubated with CellMask actin-tracking green and tubulin-tracker deep red (Thermo Fisher Scientific, Germany, #A57243 and #T34077, respectively) at ratio of 1 : 1000 in FluoroBrite DMEM (Thermo Fisher Scientific, Germany, # A1896701) for 40 min in a 37 °C/5% CO_2 incubator. Cell cytoskeletons were checked before and after the drug loading with fluorescence microscopy. ESI Fig. S17 and S18† depict the effect of the drugs on the cell cytoskeleton and the selected cells for AFM measurements.

4.3.2 Plectin siRNA transfection. Plectin siRNA(h) (#sc-29453) was received from Santa Cruz Biotechnology, Inc, Dallas Texas. The MCF10a cells were seeded on two, 1 cm size diameter coverslips in each well of a six well tissue culture plate (2×10^5 cells per well), and they were incubated until they reached 30–50% confluency. The MCF10a cells were transfected to target plectin based on the provider protocol. For each transfection 10 μl of siRNA duplex was diluted in 90 μl siRNA transfection medium (Santa Cruz Biotechnology, Inc, Dallas Texas, #sc-36868) in a vial, and 6 μl siRNA transfection reagent (Santa Cruz Biotechnology, Inc, Dallas Texas, #sc-29528) was diluted in 94 μl transfection medium in another vial. Later the first solution was added into the second vial, mixed well, and incubated at room temperature for 45 min. The culture cell coverslips were introduced to a new well plate for excluding the extra cells on the former culture plate in transfection. Cells were washed with 2 ml transfection medium and immersed in 800 μl transfection medium with no serum and antibiotics. 200 μl transfection solution was added drop-wise to each well covering the whole surface. The cells were incubated with the solution for 7 h. Next, 1 ml of 2× serum and antibiotic supplemented DMEM/F12 medium were added. After 24 h incubation, the solution was aspirated, and cells were fed with fresh normal growth medium. The cells were measured for the plectin level by western blot analysis for 24–48–72 h after the addition of fresh normal medium. Based on the results the best timepoints to measure the effect of plectin knockdown was 48 hours post-transfection (ESI Fig. S19,† plectin knockdown western blots). Transfection efficiency control tests were carried out using fluorescein conjugated control siRNA (Santa Cruz Biotechnology, Inc, Dallas Texas, #sc-44239). We note that the first round of controls with 6 μl siRNA duplex did not give a satisfactory plectin knockdown, but the high concentration of 10 μl siRNA duplex led to cell loss after 72 h of transfection.

Moreover, a separate round of transfection was performed with the optimized parameters and at 48 h after adding the fresh medium to the cells, they were characterized with AFM.

4.3.3 Nucleus isolation. Cells from both cell lines were cultured to 90% confluency. They were washed off with ice-cold PBS, and the culture dish was placed afterwards on ice, the cells were scraped off the dish while being immersed in 1 ml PBS, and they were transferred to a 1.5 ml centrifuge tube. They were centrifuged for 5–10 s at 10 000 rpm. The supernatant was discarded, and the cells were resuspended in 900 μl of ice-cold PBS containing 0.1% NP-40. The cell suspension was triturated with a pipette. They were centrifuged again for 5–10 s at 10 000 rpm and the last two steps were repeated for another round. After discarding the supernatant, isolated nuclei were resuspended in 100 μl buffer A2 (TEA 20 nM, KCl 30 mM, $MgCl_2$ 10 mM, sucrose 0.25 M, PMSF 1 : 100).

4.4 Atomic force microscopy imaging

4.4.1 PeakForce tapping quantitative mechanical mapping AFM. We obtained AFM images in the PeakForce tapping mode using a Bruker Icon atomic force microscope (Bruker AXS, Santa Barbara, CA). The deflection *versus* *z*-piezo position curves can be transformed into force *versus* indentation (FD) curves knowing the force constant of the cantilever and calibrating the inverse optical lever sensitivity on a stiff sapphire sample. Subsequently the FD curves can be fit by the Hertz/Sneddon/DMT model that provides a relationship between the sensed force by a conical indenter and the sample deformation as follows:

$$F_L = \frac{2}{\pi}\frac{E}{1-\upsilon^2}\tan(\alpha)\delta^2, \quad (3)$$

where F_L is the applied load, E the elastic modulus of the sample, υ the sample's Poisson ratio (0.3), α the half opening angle of the cone and δ the indentation depth. We used cantilevers with nominal force constants of 0.02 N m^{-1} (rectangular-shaped microlevers, MLCT-BIO-DC-B, non-conductive silicon nitride from Bruker) to gently acquire the elastic modulus of the cells for the high-resolution cell cluster spectroscopy. To obtain a more precise value of the force constant we calibrated using the thermal noise method.[88] The corresponding cantilever tip shape was pyramidal with a nominal tip radius R = 20 nm and a half-opening cone angle of α = 35°. The fundamental flexural resonant frequency of MLCT-BIO-DC-B cantilevers in cell medium was $f_{0,\ \mathrm{flex}} \approx 1.5$ kHz. AFM images were taken in CO_2-independent medium (Thermo Fisher Scientific, Germany, Gibco #18045088) to keep the risk of cell death to a minimum due to a pH value change of the medium during the measurement. PeakForce tapping mode was operated with a high digital resolution of 4096 × 4096-pixel for approximately 12 hours per image at a scan rate of 0.1 Hz for scan sizes of 91 × 91 μm^2. Consequently, the lateral resolution achieved in each image was approximately 22 nm per pixel. In persistence length measurements, *in situ* SNL cantilevers (triangular shaped microlevers, SNL-A, non-conductive sharp silicon nitride from Bruker) with a nominal force constant of 0.35 N m^{-1}, a sharp tip radius size of 2 nm and a nominal flexural resonance frequency in air of 65 kHz were used for high resolution imaging of MT filaments in fixed cells.

4.4.2 Force–volume mapping in combination with fluorescence imaging. Force–volume-mapping was performed using a Nanowizard II atomic force microscope (JPK instruments AG, Berlin, Germany) in combination with the optical stand of Zeiss Axio Observer Z1 (Carl Zeiss GmbH, Oberkochen, Germany). Force volume mapping is a linear ramp technique with which a complete force–distance curve is recorded at each pixel. Soft cantilevers with a nominal force constant of 0.06 N m^{-1} (triangular shaped microlevers, SNL-D, non-conductive sharp silicon nitride from Bruker), a nominal flexural resonance frequency in air of 18 kHz and a sharp tip radius size of 2 nm were used for measuring the mechanical properties and performing spectroscopy of the cells. The inverse optical lever sensitivity of the AFM setup was determined using a single force–distance curve on the glass substrate (coverslip) of the cells in DMEM and the cantilever spring constant was calibrated as mentioned in the PeakForce

tapping section. For stiffness tomography measurements, the trigger point was set at 1 nN, the *z*-length was 3 μm, extend time was 30 s, and the maximum sample rate was 16 000 Hz, for a grid size of 30 × 30 μm^2 with 512 × 512 point. Later, the whole map was processed with a MATLAB code to achieve the stiffness tomography as follows. In the first step, the baseline tilt was corrected by fitting a line in the data intervals between 50% and 99% of *z*-piezo values. The contact point was estimated as the *z*-piezo position and upon further approach the force stays in the positive (repulsive) interaction regime. Furthermore, the distance between the tip and sample and indentation into the sample were calculated based on the difference between cantilever deflection and *z*-piezo position. We stepwise calculated the cell stiffness with intervals of 5 nm containing four data points in each interval (see a representative F-ind curve trace trajectory, fit to the Herz–Sneddon model for each of its 5 nm intervals in ESI Fig. S20†). We show cross sections through the cell stiffness tomography in the *xz*-plane in order to present the cell's cytoskeleton component resistance under compression force and its network integrity.

For comparative analyses of the stiffness values of control measurements acquired by F–V mapping in this study, the trigger point was set at 2 nN for achieving a large indentation range, the *z*-length was 3 μm, time was extended to 90 s, and the maximum sample rate was 16 000 Hz, for a grid size of 30 × 30 μm^2 with 512 × 512 point. All the global elastic modulus values were ascertained by cumulative local elastic modulus values obtained from 4096 F–d curves measured on each cell or nucleus. For extracting the elastic modulus values the bottom effect correction was applied based on the cell topography according to ref. 64 implemented in the MATLAB code.

As the elastic modulus distributions were skewed with extreme outliers, we reported the median and mode values for an appropriate measure of the center of the data.

4.5 Confocal fluorescence microscopy imaging

Cells were imaged using a Leica SP5 II confocal microscope (Leica, Wetzlar, Germany), equipped with a 100× HCX PL Apo CS objective lens with an NA of 1.4. Alexa 488 was detected using 488 nm laser excitation and a spectral detection window of 526–558 nm. Alexa 594 was detected using 561 nm laser excitation and a spectral detection range between 570 and 680 nm. DAPI was recorded using 405 nm laser excitation and detection between 415 and 480 nm. All channels used the AOBS for the separation of excitation and emission wavelengths. Images were recorded using constant detector settings and a pixel size of 101 nm. The plane spacing in *z* was system optimized and set to approximately 300 nm. To prevent spectral cross contamination the images were recorded in two sequences.

4.6 Western blot

BT20 and MCF10A cells were grown in T75 flasks and harvested by trypsination. After cell counting the pellets were lysed in RIPA buffer (50 mM Tris-HCL pH 8.0, 1% NP-40, 0.5% sodium-deoxycholate, 150 mM NaCl, 1 mM EDTA, 0.1% SDS, 1 mM PMSF, 1 mM Na_3VO_4 and 1 mM NaF) at a density of 5.8 × 10^6 cells per ml, followed by 10 time shearing through a G21 needle. Protein concentrations were determined by the Pierce 660 nm protein-assay (Thermo Fisher) and the indicated amounts of total protein were loaded on a 12% PAA gel. After transfer to nitrocellulose (Trans-Blot Turbo, Biorad) the equal loading was controlled with Ponceau S (Thermo Fisher) and the membrane was blocked in 1% BSA in PBS for 30 min. Primary antibodies (mouse-anti-a-tubulin (clone DM1A, 1 : 5000) and mouse-anti-actin (clone AC-40, 1 : 2000), both from Sigma Aldrich) were added and incubated for 1 hour at room temperature. For the detection of the bound antibodies goat anti-mouse-IgG-Cy 5 (Amersham, 1 : 5000) was added and incubated again for 1 hour at room temperature. The bands were quantified using an Amersham AI600 imager. Experiments were performed with two biological and two technical replicates each.

4.7 Statistical analyses

4.7.1 Image processing and analysis. AFM image processing and analyses were performed with the software Nanoscope Analysis 1.8 (Bruker AXS, Santa Barbara, CA), JPKSPM data processing (JPK instruments AG) and Gwyddion 2.54 (Department of Nanometrology, Czech Metrology Institute, Czech Republic). Data processing and fitting of the elastic moduli and deformation values to Gaussian distribution were performed with Igor pro 6.37 (WaveMetrics, Inc, Portland, OR). Violin plots of kernel smoothed density estimates of the stiffness were produced using a MATLAB code (the width of the violin in axis space is by default 0.3 and the bandwidth of the kernel density estimate was between 10% and 40% of the data range). Mann–Whitney *U*-test and Kruskal–Wallis *H*-test were performed and to identify the specific pairs with significant differences, a Dunn–Bonferroni test was conducted and analyses were carried out using the statistics software Prism version 10 (June 2023). Ridgeline plots of kernel smoothed density estimates of the stiffness were produced using Origin (version 2023b) which was set to Scott bandwidth.[89] Details about the image size and image resolution can be found in the atomic force microscopy imaging section.

4.7.2 Persistence length assessment. Cells were incubated with 5 μl ml^{-1} cytochalasin-D for 30 min and instantly fixed with 3.7% formaldehyde diluted in PBS for 15 min followed by 10 min permeabilization with −20 °C methanol to dissolve the bilipid layer and air dried. These steps were taken to have direct access to the MTs in cells *in situ.* Fig. 9a–c show a schematic illustration of chain conformations depending on l_p and *L*. We used the WLC freely jointed chain model to fit the MTs for measuring the persistence length. Fig. 9d illustrates the end-to-end bending mode approach with the deviation size δ from the straight line of correlation length ξ and Fig. 9e illustrates the angular analysis that determines the l_p from the cosine correlation of tangent angles θ along the characteristic length of (s).

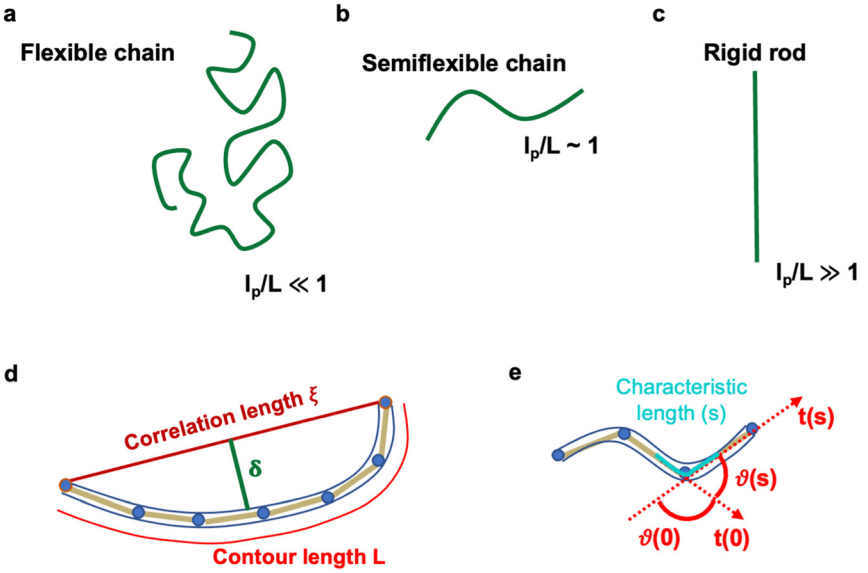

Fig. 9 Schematic illustration of chain conformations depending on l_p and L. (a) Flexible chain, (b) semiflexible chain, and (c) rigid rod. WLC models with (d) end-to-end bending mode fitting and (e) cosine correlation of tangent angles θ along the segment (s).

The correlation length ξ and deviation size δ were measured from the total planar distance, and angles θ were measured from the azimuth ϕ, with the distance tool in Gwyddion 2.54 (Department of Nanometrology, Czech Metrology Institute, Czech Republic). The characteristic length (s) was measured by drawing a mask, with the same width of the filament, over the length scale with which the decay occurs. Using the Gwyddion statistical quantities tool, we found the masked projected area. Dividing this area by the filament width (mask width, ~25 nm for single MT and ~100 for MT-bundles) granted us a good estimate of the characteristic planar length.

Data availability

The data that support the findings of this study are available within the paper and its ESI and ESI files.† Raw data are available from the corresponding author on request.

Author contributions

A. A. and A. R. performed the experimental investigations. A. A. conceived the concept, designed the project, analyzed the data, carried out the theoretical calculations, and together with R. W. S., M. C. C., A. R., and C. D. discussed the results and prepared this manuscript.

Conflicts of interest

The authors declare no competing interests.

Acknowledgements

The authors thank Dr Heiko Haschke, Bruker's director of BioAFM, and Dr Alexander Dulebo, Bruker's Bio sales Application Engineer, for their scientific support, Dr Martin Dehnert for the MATLAB codes, and Dr Hector Romero for data illustration support.

References

1 D. Hanahan and R. A. Weinberg, Hallmarks of Cancer: The Next Generation, *Cell*, 2011, **144**(5), 646–674.
2 C. Vicente-Duenas, *et al.*, Epigenetic Priming in Cancer Initiation, *Trends Cancer*, 2018, **4**(6), 408–417.
3 S. A. Stacker, *et al.*, Lymphangiogenesis and lymphatic vessel remodelling in cancer, *Nat. Rev. Cancer*, 2014, **14**(3), 159–172.
4 R. S. Watnick, The Role of the Tumor Microenvironment in Regulating Angiogenesis, *Cold Spring Harbor Perspect. Med.*, 2012, **2**(12), a006676.
5 J. Alexander and E. Cukierman, Stromal dynamic reciprocity in cancer: intricacies of fibroblastic-ECM interactions, *Curr. Opin. Cell Biol.*, 2016, **42**, 80–93.
6 F. R. Greten and S. I. Grivennikov, Inflammation and Cancer: Triggers, Mechanisms, and Consequences, *Immunity*, 2019, **51**(1), 27–41.
7 C. H. Stuelten, C. A. Parent and D. J. Montell, Cell motility in cancer invasion and metastasis: insights from simple model organisms, *Nat. Rev. Cancer*, 2018, **18**(5), 296–312.
8 A. S. Piotrowski-Daspit, J. Tien and C. M. Nelson, Interstitial fluid pressure regulates collective invasion in

engineered human breast tumors via Snail, vimentin, and E-cadherin, *Integr. Biol.*, 2016, **8**(3), 319–331.
9 M. Lintz, A. Munoz and C. A. Reinhart-King, The Mechanics of Single Cell and Collective Migration of Tumor Cells, *J. Biomech. Eng.: Trans. ASME*, 2017, **139**(2), 0210051–0210059.
10 A. Fritsch, *et al.*, Are biomechanical changes necessary for tumour progression?, *Nat. Phys.*, 2010, **6**(10), 730–732.
11 S. Suresh, Biomechanics and biophysics of cancer cells, *Acta Biomater.*, 2007, **3**(4), 413–438.
12 C. T. Mierke, The fundamental role of mechanical properties in the progression of cancer disease and inflammation, *Rep. Prog. Phys.*, 2014, **77**(7), 076602.
13 M. E. Grady, R. J. Composto and D. M. Eckmann, Cell elasticity with altered cytoskeletal architectures across multiple cell types, *J. Mech. Behav. Biomed. Mater.*, 2016, **61**, 197–207.
14 R. Omidvar, *et al.*, Atomic force microscope-based single cell force spectroscopy of breast cancer cell lines: An approach for evaluating cellular invasion, *J. Biomech.*, 2014, **47**(13), 3373–3379.
15 M. M. Yallapu, *et al.*, The Roles of Cellular Nanomechanics in Cancer, *Med. Res. Rev.*, 2015, **35**(1), 198–223.
16 M. Lekka, *et al.*, Cancer cell detection in tissue sections using AFM, *Arch. Biochem. Biophys.*, 2012, **518**(2), 151–156.
17 S. E. Cross, *et al.*, Nanomechanical analysis of cells from cancer patients, *Nat. Nanotechnol.*, 2007, **2**(12), 780–783.
18 M. Plodinec, *et al.*, The nanomechanical signature of breast cancer, *Nat. Nanotechnol.*, 2012, **7**(11), 757–765.
19 M. Prabhune, *et al.*, Comparison of mechanical properties of normal and malignant thyroid cells, *Micron*, 2012, **43**(12), 1267–1272.
20 C. Alibert, B. Goud and J. B. Manneville, Are cancer cells really softer than normal cells?, *Biol. Cell*, 2017, **109**(5), 167–189.
21 A. Kubiak, *et al.*, Nanomechanics in Monitoring the Effectiveness of Drugs Targeting the Cancer Cell Cytoskeleton, *Int. J. Mol. Sci.*, 2020, **21**(22), 8786.
22 J. R. Ramos, *et al.*, The softening of human bladder cancer cells happens at an early stage of the malignancy process, *Beilstein J. Nanotechnol.*, 2014, **5**, 447–457.
23 A. Calzado-Martin, *et al.*, Effect of Actin Organization on the Stiffness of Living Breast Cancer Cells Revealed by Peak-Force Modulation Atomic Force Microscopy, *ACS Nano*, 2016, **10**(3), 3365–3374.
24 N. Gal and D. Weihs, Intracellular Mechanics and Activity of Breast Cancer Cells Correlate with Metastatic Potential, *Cell Biochem. Biophys.*, 2012, **63**(3), 199–209.
25 K. Mandal, *et al.*, Mapping intracellular mechanics on micropatterned substrates, *Proc. Natl. Acad. Sci. U. S. A.*, 2016, **113**(46), E7159–E7168.
26 M. Kavallaris, Microtubules and resistance to tubulin-binding agents, *Nat. Rev. Cancer*, 2010, **10**(3), 194–204.
27 G. Ferrandina, *et al.*, Class III beta-tubulin overexpression is a marker of poor clinical outcome in advanced ovarian cancer patients, *Clin. Cancer Res.*, 2006, **12**(9), 2774–2779.
28 J. A. McCarroll, *et al.*, beta III-Tubulin Is a Multifunctional Protein Involved in Drug Sensitivity and Tumorigenesis in Non-Small Cell Lung Cancer, *Cancer Res.*, 2010, **70**(12), 4995–5003.
29 P. P. Gan and M. Kavallaris, Tubulin-Targeted Drug Action: Functional Significance of Class II and Class IVb beta-Tubulin in Vinca Alkaloid Sensitivity, *Cancer Res.*, 2008, **68**(23), 9817–9824.
30 S. Mozzetti, *et al.*, Molecular Mechanisms of Patupilone Resistance, *Cancer Res.*, 2008, **68**(24), 10197–10204.
31 M. A. H. Albahde, *et al.*, The Role of Microtubules in Pancreatic Cancer: Therapeutic Progress, *Front. Oncol.*, 2021, **11**, 640863.
32 C. H. Lu, *et al.*, Increased alpha-Tubulin1b Expression Indicates Poor Prognosis and Resistance to Chemotherapy in Hepatocellular Carcinoma, *Dig. Dis. Sci.*, 2013, **58**(9), 2713–2720.
33 J. A. McCarroll, *et al.*, beta III-Tubulin: A novel mediator of chemoresistance and metastases in pancreatic cancer, *Oncotarget*, 2015, **6**(4), 2235–2249.
34 G. Sharbeen, *et al.*, Delineating the Role of beta IV-Tubulins in Pancreatic Cancer: beta IVb- Tubulin Inhibition Sensitizes Pancreatic Cancer Cells to Vinca Alkaloids, *Neoplasia*, 2016, **18**(12), 753–764.
35 K. Soucek, *et al.*, Normal and prostate cancer cells display distinct molecular profiles of alpha-tubulin posttranslational modifications, *Prostate*, 2006, **66**(9), 954–965.
36 A. Mialhe, *et al.*, Tubulin detyrosination is a frequent occurrence in breast cancers of poor prognosis, *Cancer Res.*, 2001, **61**(13), 5024–5027.
37 C. Kato, *et al.*, Low expression of human tubulin tyrosine ligase and suppressed tubulin tyrosination/detyrosination cycle are associated with impaired neuronal differentiation in neuroblastomas with poor prognosis, *Int. J. Cancer*, 2004, **112**(3), 365–375.
38 M. M. Magiera, *et al.*, Tubulin Posttranslational Modifications and Emerging Links to Human Disease, *Cell*, 2018, **173**(6), 1323–1327.
39 K. M. R. Bhat and V. Setaluri, Microtubule-associated proteins as targets in cancer chemotherapy, *Clin. Cancer Res.*, 2007, **13**(10), 2849–2854.
40 C. Schroeder, *et al.*, Aberrant expression of the microtubule-associated protein tau is an independent prognostic feature in prostate cancer, *BMC Cancer*, 2019, **19**, 193.
41 J. Y. Luo, *et al.*, Expression of Microtubule-Associated Proteins in Relation to Prognosis and Efficacy of Immunotherapy in Non-Small Cell Lung Cancer, *Front. Oncol.*, 2021, **11**, 680402.
42 A. M. Collinsworth, *et al.*, Apparent elastic modulus and hysteresis of skeletal muscle cells throughout differentiation, *Am. J. Physiol.: Cell Physiol.*, 2002, **283**(4), C1219–C1227.
43 K. Nagayama and T. Matsumoto, Contribution of actin filaments and microtubules to quasi-in situ tensile properties and internal force balance of cultured smooth muscle cells on a substrate, *Am. J. Physiol.: Cell Physiol.*, 2008, **295**(6), C1569–C1578.

44 H. Kubitschke, *et al.*, Actin and microtubule networks contribute differently to cell response for small and large strains, *New J. Phys.*, 2017, **19**, 093003.
45 C. P. Brangwynne, *et al.*, Microtubules can bear enhanced compressive loads in living cells because of lateral reinforcement, *J. Cell Biol.*, 2006, **173**(5), 733–741.
46 A. Amiri, *et al.*, Structural analysis of healthy and cancerous epithelial-type breast cells by nanomechanical spectroscopy allows us to obtain peculiarities of the skeleton and junctions, *Nanoscale Adv.*, 2019, **1**(12), 4853–4862.
47 A. Amiri, F. D. Hastert and C. Dietz, Carcinomas with Occult Metastasis Potential: Diagnosis/Prognosis Accuracy Improvement by Means of Force Spectroscopy, *Adv. Biosyst.*, 2020, **4**(7), 2000042.
48 A. Amiri, *et al.*, Reliability of cancer cell elasticity in force microscopy, *Appl. Phys. Lett.*, 2020, **116**(8), 083701.
49 G. Wiche, Role of plectin in cytoskeleton organization and dynamics, *J. Cell Sci.*, 1998, **111**, 2477–2486.
50 T. M. Svitkina, A. B. Verkhovsky and G. B. Borisy, Plectin sidearms mediate interactions of intermediate filaments with microtubules and other components of the cytoskeleton, *Biol. Bull.*, 1998, **194**(3), 409–410.
51 M. J. Castanon, *et al.*, Plectin-intermediate filament partnership in skin, skeletal muscle, and peripheral nerve, *Histochem. Cell Biol.*, 2013, **140**(1), 33–53.
52 T. Matsubara, *et al.*, Plectin stabilizes microtubules during osteoclastic bone resorption by acting as a scaffold for Src and Pyk2, *Bone*, 2020, **132**, 115209.
53 R. G. Valencia, *et al.*, Intermediate filament-associated cytolinker plectin 1c destabilizes microtubules in keratinocytes, *Mol. Biol. Cell*, 2013, **24**(6), 768–784.
54 K. Mado, *et al.*, On the role of tubulin, plectin, desmin, and vimentin in the regulation of mitochondrial energy fluxes in muscle cells, *Am. J. Physiol.: Cell Physiol.*, 2019, **316**(5), C657–C667.
55 E. Ortega, *et al.*, The Structure of the Plakin Domain of Plectin Reveals an Extended Rod-like Shape, *J. Biol. Chem.*, 2016, **291**(36), 18643–18662.
56 K. Andra, *et al.*, Targeted inactivation of plectin reveals essential function in maintaining the integrity of skin, muscle, and heart cytoarchitecture, *Genes Dev.*, 1997, **11**(23), 3143–3156.
57 G. Wiche, Plectin-Mediated Intermediate Filament Functions: Why Isoforms Matter, *Cells*, 2021, **10**(8), 2154.
58 F. Nedelec, T. Surrey and E. Karsenti, Self-organisation and forces in the microtubule cytoskeleton, *Curr. Opin. Cell Biol.*, 2003, **15**(1), 118–124.
59 E. Frixione and M. Hernández, Structural Organization of Cells – The Cytoskeleton, in *Comprehensive Biotechnology*, Academic Press, 2nd edn, 2011.
60 A. Hallou, J. Jennings and A. J. Kabla, Tumour heterogeneity promotes collective invasion and cancer metastatic dissemination, *R. Soc. Open Sci.*, 2017, **4**(8), 161007.
61 A. Marusyk, V. Almendro and K. Polyak, Intra-tumour heterogeneity: a looking glass for cancer?, *Nat. Rev. Cancer*, 2012, **12**(5), 323–334.
62 I. Dagogo-Jack and A. T. Shaw, Tumour heterogeneity and resistance to cancer therapies, *Nat. Rev. Clin. Oncol.*, 2018, **15**(2), 81–94.
63 X. X. Sun and Q. Yu, Intra-tumor heterogeneity of cancer cells and its implications for cancer treatment, *Acta Pharmacol. Sin.*, 2015, **36**(10), 1219–1227.
64 P. D. Garcia and R. Garcia, Determination of the Elastic Moduli of a Single Cell Cultured on a Rigid Support by Force Microscopy, *Biophys. J.*, 2018, **114**(12), 2923–2932.
65 A. Kubiak, *et al.*, Stiffening of DU145 prostate cancer cells driven by actin filaments - microtubule crosstalk conferring resistance to microtubule-targeting drugs, *Nanoscale*, 2021, **13**(12), 6212–6226.
66 A. C. Raymond, *et al.*, Unbiased peptoid combinatorial cell screen identifies plectin protein as a potential biomarker for lung cancer stem cells, *Sci. Rep.*, 2019, **9**, 14954.
67 S. M. Perez, L. T. Brinton and K. A. Kelly, Plectin in Cancer: From Biomarker to Therapeutic Target, *Cells*, 2021, **10**(9), 2246.
68 T. Niwa, *et al.*, BRCA2 interacts with the cytoskeletal linker protein plectin to form a complex controlling centrosome localization, *Cancer Sci.*, 2009, **100**(11), 2115–2125.
69 P. Fuchs and G. Wiche, *Encyclopedia of Biological Chemistry*, Academic Press, 2nd edn, 2013.
70 G. Wiche, *et al.*, Occurrence and immunolocalization of plectin in tissues, *J. Cell Biol.*, 1983, **97**(3), 887–901.
71 Y. Gebremichael, J. W. Chu and G. A. Voth, Intrinsic bending and structural rearrangement of tubulin dimer: Molecular dynamics simulations and coarse-grained analysis, *Biophys. J.*, 2008, **95**(5), 2487–2499.
72 J. M. Cleary and W. O. Hancock, Molecular mechanisms underlying microtubule growth dynamics, *Curr. Biol.*, 2021, **31**(10), R560–R573.
73 T. Muller-Reichert, *et al.*, Structural changes at microtubule ends accompanying GTP hydrolysis: Information from a slowly hydrolyzable analogue of GTP, guanylyl (alpha,beta) methylenediphosphonate, *Proc. Natl. Acad. Sci. U. S. A.*, 1998, **95**(7), 3661–3666.
74 L. M. Rice, E. A. Montabana and D. A. Agard, The lattice as allosteric effector: Structural studies of alpha beta- and gamma-tubulin clarify the role of GTP in microtubule assembly, *Proc. Natl. Acad. Sci. U. S. A.*, 2008, **105**(14), 5378–5383.
75 O. Kratky and G. Porod, RONTGENUNTERSUCHUNG GELOSTER FADENMOLEKULE, *Recl.: J. R. Neth. Chem. Soc.*, 1949, **68**(12), 1106–1122.
76 C. P. Broedersz and F. C. MacKintosh, Modeling semiflexible polymer networks, *Rev. Mod. Phys.*, 2014, **86**(3), 995–1036.
77 K. Y. Jia and X. H. Liu, Measuring the flexural rigidity of actin filaments and microtubules from their thermal fluctuating shapes: A new perspective, *J. Mech. Phys. Solids*, 2017, **101**, 64–92.
78 G. Lamour, *et al.*, Easyworm: an open-source software tool to determine the mechanical properties of worm-like chains, *Source Code Biol. Med.*, 2014, **9**(1), 16.

79 A. Marantan and L. Mahadevan, Mechanics and statistics of the worm-like chain, *Am. J. Phys.*, 2018, **86**(2), 86–94.
80 F. Gittes, *et al.*, Flexural rigidity of microtubules and actin-filaments measured from thermal fluctuations in shape, *J. Cell Biol.*, 1993, **120**(4), 923–934.
81 M. E. Janson and M. Dogterom, A bending mode analysis for growing microtubules: Evidence for a velocity-dependent rigidity, *Biophys. J.*, 2004, **87**(4), 2723–2736.
82 M. E. Janson and M. Dogterom, Scaling of microtubule force-velocity curves obtained at different tubulin concentrations, *Phys. Rev. Lett.*, 2004, **92**(24), 248101.
83 A. Kis, *et al.*, Nanomechanics of microtubules, *Phys. Rev. Lett.*, 2002, **89**(24), 248101.
84 S. Kasas, *et al.*, Mechanical properties of microtubules explored using the finite elements method, *ChemPhysChem*, 2004, **5**(2), 252–257.
85 F. Pampaloni, *et al.*, Thermal fluctuations of grafted microtubules provide evidence of a length-dependent persistence length, *Proc. Natl. Acad. Sci. U. S. A.*, 2006, **103**(27), 10248–10253.
86 C. Heussinger, M. Bathe and E. Frey, Statistical mechanics of semiflexible bundles of wormlike polymer chains, *Phys. Rev. Lett.*, 2007, **99**(4), 048101.
87 M. G. L. van den Heuvel, M. R. de Graaff and C. Dekker, Microtubule curvatures under perpendicular electric forces reveal a low persistence length, *Proc. Natl. Acad. Sci. U. S. A.*, 2008, **105**(23), 7941–7946.
88 H. J. Butt and M. Jaschke, Calculation of thermal noise in atomic-force microscopy, *Nanotechnology*, 1995, **6**(1), 1–7.
89 D. W. Scott, Optimal and data-based histograms, *Biometrika*, 1979, **66**(3), 605–610.